nature structural & molecular biology

Article

https://doi.org/10.1038/s41594-025-01615-4

A conserved coupling of transcriptional ON and OFF periods underlies bursting dynamics

Received: 13 June 2024

Accepted: 5 June 2025

Published online: 15 July 2025

Check for updates

Po-Ta Chen[1,4], Michal Levo[1,2,4], Benjamin Zoller[1,3,4] & Thomas Gregor[1,3]

Transcription commonly occurs in bursts, with alternating productive (ON) and quiescent (OFF) periods determining mRNA production rates. However, how bursting dynamics regulate transcription is not well understood. Here, we conduct real-time measurements of endogenous transcriptional bursting with single-mRNA sensitivity. Using the diverse transcriptional activities present in early *Drosophila* embryos, we find stringent relationships between bursting parameters. Specifically, ON and OFF durations are tightly coupled, and each level of gene activity is associated with a characteristic combination of these periods. Lowly transcribing alleles primarily adjust OFF periods (burst frequency), while highly transcribing alleles tune ON periods (burst size). These relationships persist across developmental stages, body-axis positions, *cis*-regulatory or *trans*-regulatory perturbations and bursting dynamics observed in other species. Our findings suggest a mechanistic constraint that governs bursting dynamics, challenging the view that regulatory processes independently control distinct parameters.

Eukaryotic transcriptional regulation is an inherently dynamic and stochastic process, orchestrated by a series of molecular events governing productive transcription initiation by individual RNA polymerases (Pol II complexes)[1,2]. This process culminates in nascent RNA synthesis, which shapes protein production and thus dictates cellular identity and behavior in space and time. Consequently, revealing the fundamental principles underpinning transcriptional dynamics is paramount for understanding and predicting cellular phenotypes.

Research on various biological systems, from yeast to mammalian cells, has revealed that transcription occurs in bursts. These bursts involve the release of multiple Pol II complexes during an active phase, known as the 'ON' period, followed by a quiescent 'OFF' period[3–9]. However, several critical questions remain unanswered regarding how the regulation of bursting kinetics determines mRNA production and transcriptional dynamics across developmental time and cell types; whether the transcription rate is primarily regulated by adjusting the ON or OFF durations, the initiation rate (that is, the rate of Pol II release during active phases) or a combination of these parameters; what spectrum of parameters is used by tightly regulated genes, such as developmental genes; whether different genes use distinct bursting strategies; and whether these strategies vary across space (tissue-specific) and time, or how they depend on various regulatory factors.

One hypothesis that has emerged from previous work suggests that different regulatory determinants, including transcription factor binding, *cis*-regulatory elements, nucleosome occupancy, histone modification, Pol II pausing and enhancer–promoter interactions, may influence distinct aspects of bursting dynamics[10–19]. For instance, it has been proposed that enhancers primarily impact burst frequency, whereas promoters mostly affect burst size[20–22]. However, integrating diverse observations into a unified and quantitatively predictive understanding of transcriptional control through bursting dynamics has proven challenging.

[1]Joseph Henry Laboratories of Physics & Lewis-Sigler Institute for Integrative Genomics, Princeton University, Princeton, NJ, USA. [2]Department of Biochemistry and Molecular Biophysics, Columbia University, New York, NY, USA. [3]Department of Stem Cell and Developmental Biology, CNRS UMR3738 Paris Cité, Institut Pasteur, Paris, France. [4]These authors contributed equally: Po-Ta Chen, Michal Levo, Benjamin Zoller. e-mail: tg2@princeton.edu

https://doi.org/10.1038/s41594-025-01615-4

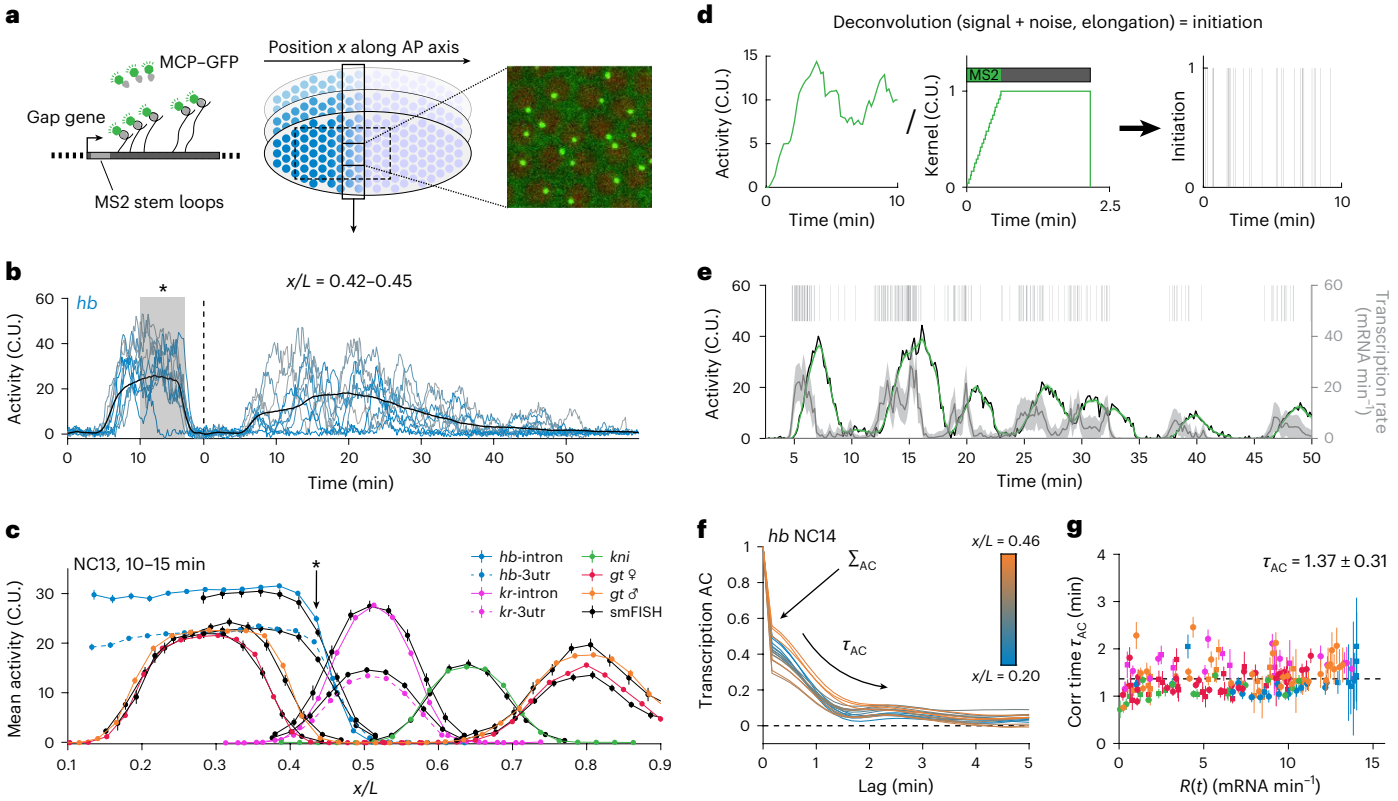

Fig. 1 | Live single-cell transcription rate measurements of endogenous gap genes. a, Live fluorescence imaging of nascent transcripts using MS2 stem-loops measures single-allele transcriptional activity (green hotspots) along the anterior–posterior (AP) axis of the fly embryo (see Extended Data Fig. 1a and Methods). MCP, MS2 coat protein. **b**, Transcription time series for ten alleles (blue) of the gap gene *hunchback* (*hb*) at position $x/L = 0.435 \pm 0.010$ sampled every 10 s. Low embryo-to-embryo variability (Supplementary Fig. 1g) enables pooling alleles from multiple spatially and temporally aligned embryos ($n = 10$–20) to average over 200–350 alleles at a given position (black). **c**, Calibration of transcriptional activity in absolute units performed by matching mean spatial activity profiles from previously calibrated fixed smFISH measurements[23] (black) with 5 min interval averages (gray shade in **b**) of live time series at each AP position (color) for all examined gap genes. A single global conversion factor matches live and fixed profiles to within 5% error (Extended Data Fig. 1b), defining a unit for transcriptional activity (that is, the cytoplasmic unit, C.U.[66,67]) equivalent to a fully tagged transcript. **d**, Reconstruction of transcription initiation events from deconvolution of single-allele transcription time series. The signal is modeled as a convolution between transcription initiation events and a kernel accounting for the elongation of a single Pol II through the MS2 cassette and the gene body (using an elongation rate $K_{elo} = 1.8$ kb min^{-1}; Supplementary Fig. 2). Bayesian deconvolution is performed by sampling from the posterior distribution of possible configuration of initiation events given the measured activity and measurement noise (Extended Data Fig. 1e,f). **e**, Example deconvolved initiation configuration (gray bars, top) and corresponding reconstructed signal (green) from a single-allele transcription time series (black). Single-allele transcription rate (gray) is estimated by counting the number of initiation events within 10 s intervals for a given sampled configuration and averaged over 1,000 such configurations. The displayed solid line and envelope for transcription rate (gray) and reconstructed signal (green) correspond to the mean and 1 s.d. of the posterior distribution. **f**, Autocorrelation (AC) functions of single allele *hb* transcription rates averaged over time for different positions along the AP axis (color). AC functions are normalized by the variance; uncorrelated ($1-\Sigma_{AC}$) and time-correlated (Σ_{AC}) components of the rate fluctuations are highlighted (see Extended Data Fig. 5). **g**, Correlation time τ_{AC} (from fitted exponentials; see Methods) of the single-allele transcription rate as a function of mean transcription rate R (color-coded as in **c**, with NC13 (squares) and NC14 (circles)). The dashed line corresponds to overall mean correlation time $\bar{\tau}_{AC} = 1.37 \pm 0.31$ min. Error bars, 68% confidence intervals.

Our previous study[23], which relied on inference from a static snapshot of mRNA abundance, raised the possibility of a simple and unified control of bursting kinetics, even in complex developmental systems. Specifically, mRNA abundance of key developmental genes in fixed *Drosophila* embryos within a narrow developmental window (~10 min) could be accounted for by a straightforward two-state kinetic model of transcription, with a single free parameter. This motivated our current efforts to directly measure bursting dynamics rather than rely on specific kinetic assumptions to infer dynamics from a fixed sample. Moreover, we aim to assess the impact of developmental time and regulation on bursting behavior by conducting measurements throughout cell cycles and under perturbations to key regulatory determinants.

Here, we present real-time transcription measurements with single-mRNA sensitivity, characterizing the bursting dynamics of cell fate-determining genes in early *Drosophila* embryos. Our findings reveal tight relationships between bursting parameters, including the coupling of ON and OFF periods (or burst size and frequency), suggesting that these parameters are not independently regulated but arise from coordinated processes. Gene activity levels are achieved through specific combinations of ON and OFF durations, regardless of gene identity or spatiotemporal context. Low-activity alleles primarily adjust OFF periods (modulating frequency), while mid-activity to high-activity alleles adjust ON periods (modulating size). This coupling holds across diverse regulatory landscapes, as we demonstrate with *cis* and *trans* perturbations, and appears broadly conserved in other organisms. As these dependencies do not straightforwardly stem from known molecular mechanisms of transcription initiation, our findings challenge current models and provide a framework for future investigations into the process of mRNA production.

Results

Instantaneous single-allele transcription rate measurements

We developed a quantitative approach to measure endogenous bursting dynamics at a single-allele level in living *Drosophila* embryos. To

achieve this goal, we used a versatile CRISPR-based scheme[24] to incorporate MS2 cassettes into intronic or 3′ untranslated regions (3′ UTRs) of the gap genes. These cassettes form stem-loops in the transcribed nascent RNA, which are subsequently bound by fluorescent coat proteins (Fig. 1a, Extended Data Fig. 1a and Methods)[25–28]. We used a custom-built two-photon microscope to generate fluorescence images, allowing us to capture RNA synthesis from one tagged allele per nucleus with nearly single-mRNA sensitivity (Extended Data Fig. 1b–f). Our optimized field-of-view provided 10 s interval time lapses (Fig. 1b) for hundreds of nuclei per embryo during a critical 1.5 h period of embryonic development, specifically nuclear cycles 13 (NC13) and 14 (NC14), for robust statistical analysis (Fig. 1a,b and Supplementary Videos 1–4).

We calibrated the fluorescence signal using single-molecule fluorescence in situ hybridization (smFISH) data to express our dynamic transcription measurements in terms of absolute mRNA counts (Fig. 1c, Extended Data Fig. 1b,c and Methods). This calibration, along with control lines using 3′-UTR MS2 insertions, confirms that the intronic readout of our short genes (<5 kb, including MS2 loops) is unaffected by splicing[9] (Extended Data Fig. 1a,b). Additionally, we verified the absence of bleaching during imaging, as indicated by the stability of the measured background over 1.5 h (Extended Data Fig. 1d). Lastly, we characterized our measurement noise using an interlaced MS2–PP7 dual-color reporter line, which showed a strong correlation between the two independent channels. The resulting signal-to-noise ratio is approximately 1 at one mRNA count. It increases with mean activity, confirming that our sensitivity is close to detecting individual molecules (Extended Data Fig. 1e,f).

The smFISH-based calibration, combined with nearly single-transcript sensitivity of our measurements, enabled us to reconstruct the underlying Pol II transcription initiation events for each allele using Bayesian deconvolution (Methods). The convolution kernel we used describes the fluorescent signal resulting from the release of Pol II complexes onto the gene, which subsequently engages in the elongation process[17,21] (assuming constant and deterministic elongation; Fig. 1d). For each time trace, our Bayesian approach generates multiple configurations of transcription initiation events. By averaging these configurations, we obtained a time-dependent instantaneous single-allele transcription rate, denoted $r(t)$ (Fig. 1e). Importantly, this approach also provides corresponding error estimates, which we propagated in all subsequent analyses.

Our kernel-based deconvolution approach was validated by control measurements involving dual-color tagging of the gene body, at 5′ and 3′ regions (Extended Data Fig. 2a,b and Methods). Furthermore, the dual tagging allows us to extract a Pol II elongation rate, denoted K_{elo}, which we determined to be 1.8 ± 0.1 kb min^{-1}. This value aligns with previous measurements reported in the literature[27,29] (Extended Data Fig. 2c–e).

With our approach, the extracted single-allele transcription rates are no longer masked by the Pol II elongation dwell time, unlike the directly measured intensities. Instead, they capture initiation events (that is, Pol II release for productive elongation). Consequently, these rates are independent of gene length, allowing direct comparisons across different genes. This facilitated the intriguing observation that the gap genes' average transcription rate, computed over nuclei per spatial position and time, denoted as $R = \langle r \rangle$, reaches a similar maximum of R_{max} = 14.8 ± 0.9 mRNA min^{-1} (Extended Data Fig. 3a and Supplementary Video 5). Moreover, these average transcription rates closely mirror the well-documented average protein dynamics[30]. Simple assumptions related to diffusion and lifetime, without the need for explicit post-transcriptional regulation, are sufficient to quantitatively predict protein patterns from the mean transcription rates, R (Extended Data Fig. 4 and Supplementary Video 6). Thus, in this system, the functional output, namely protein synthesis, predominantly relies on transcription regulation. Our quantitative imaging and deconvolution approach paves the way for uncovering how this regulation emerges from the single-allele transcription dynamics.

Single-allele rates point to a universal bursting regime

The gap genes exhibit spatial and temporal variation in their transcriptional activities. However, when we examine the distributions $P(r|R)$ of single-allele transcription rates r that correspond to a given mean transcription rate R, an intriguing pattern emerges. These distributions converge across different genes (Extended Data Fig. 3c and Methods), pointing to a shared transcriptional regime. We observe an abundance of non-transcribing or barely transcribing alleles for transcription rates in the low to mid-range of R, distinct from the expectation under a constitutive transcription regime. Conversely, for transcription rates in the high range of R, the distributions approach a constitutive, or Poissonian, regime (Extended Data Fig. 3d), reflecting a higher proportion of active ON alleles. These observations align with the concept of transcriptional bursting, in which alleles dynamically transition between productive ON and quiescent OFF states[3,31].

We obtain additional support for a common bursting regime when we analyze the temporal dynamics of single-allele time traces. Bursting is expected to introduce temporal correlations in transcriptional activity, reflecting the persistence of the ON and OFF periods (Extended Data Fig. 5a,b). To characterize such correlations, we compute autocorrelation functions for the deconvolved single-allele transcription rates. By using the deconvolved rates, we effectively remove the correlated component arising from Pol II elongation along the gene and isolate only the correlations stemming from the initiation and the ON–OFF switching process. When we calculate these autocorrelation functions for different anterior–posterior bins, nuclear cycles and various genes (Fig. 1f and Extended Data Fig. 5c), we find striking similarities. An initial sharp drop at our sampling timescale (~10 s) indicates the presence of uncorrelated noise, consistent with independent Pol II initiation events (Extended Data Fig. 5d). This drop is followed by a longer decay of correlated noise at a timescale denoted τ_{AC}, which we find to be confined within a 1–2 min range (Fig. 1g). The remarkable consistency of τ_{AC} across different spatial locations, genes and transcriptional activity levels (spanning R) implies the preservation of this fundamental timescale of transcription dynamics. To delve deeper into potential regularities in bursting dynamics, we next directly extract individual bursts from single-allele time traces.

Allele-ON probability is the key control parameter

From the deconvolved initiation events along individual time traces (Fig. 2a top), we identify distinct ON and OFF periods of active and inactive transcription, respectively. The ON periods are characterized by consecutive initiation events (that is, multiple Pol IIs released for productive elongation), while the OFF periods are transcriptionally inactive (Fig. 2a, bottom). To delineate the transition of an allele from an OFF to an ON state, we use a simple threshold on the moving average of the single-allele transcription rate, set to 2 mRNA min^{-1} over a 1 min window. This criterion was selected based on our detection sensitivity, allowing us to reliably detect 1–2 mRNA molecules, at the timescale derived from the autocorrelation analysis (see Methods).

To validate our method, we tested our burst-calling routine extensively on simulated data (Supplementary Figs. 1 and 2). As the true generative model is unknown, we tested our method using a subset of commonly used bursting models, including a two-state model, a three-state pause model and a six-state cycle model[9,12,17,21,32–34]. These models primarily differ in their distributions of ON and OFF periods (for example, exponential for the two-state model). A key strength of our burst-calling routine is its reliance on a minimal clustering model, which avoids explicit assumptions about these distributions. Consequently, the burst detection process is agnostic to the underlying mechanistic details. Simulations demonstrate that our approach performs robustly across a wide range of (stationary and time-dependent) kinetic parameters and model classes (Supplementary Figs. 1a–g and 2),

https://doi.org/10.1038/s41594-025-01615-4

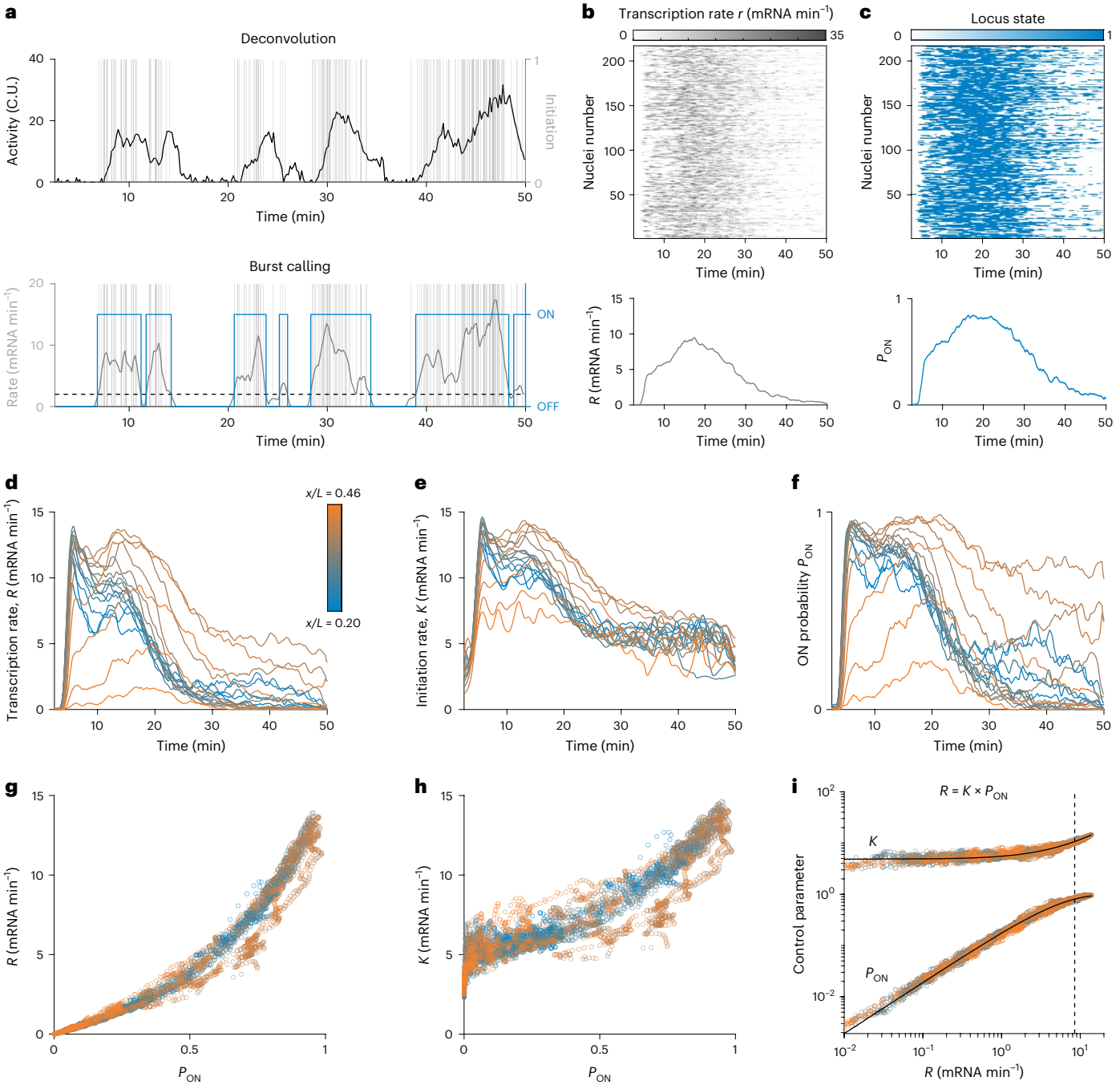

Fig. 2 | Direct estimation of bursting parameters reveals predominant control by the ON probability. a, A simple clustering procedure on single-allele transcription rate determines bursts of transcription. The rate (gray curve) is estimated using a moving window of width ~1 min over the deconvolved initiation events (gray vertical bars). A threshold at two mRNA min^{-1} (black horizontal dashed line) applied to the rate identifies individual bursts (blue curves). For tests of the burst-calling procedure on simulated data, see the Supplementary Information. **b**,**c**, Heatmaps of deconvolved single-allele transcription rates (**b**) (estimated over 10 s intervals) and of corresponding ON–OFF periods (**c**) (obtained from burst calling) as a function of time during NC14 for $n = 217$ nuclei expressing *hb*-MS2 at AP position $x/L = 0.43$. Instantaneous mean transcription parameters such as transcription rate R (**b**, bottom) and ON probability P_{ON} (**b**, bottom) are obtained by vertically averaging the heatmaps (top) over all nuclei, respectively. **d**,**f**, *Hb* transcription rate R (**d**), initiation rate K (**e**) and ON probability P_{ON} (**f**) as a function of time in NC14 (color encodes AP position). R and P_{ON} are computed as in **b** and **c**, respectively, and K is obtained by averaging the single-allele transcription rate (**b**) conditioned on the locus being ON (**c**) over all nuclei in each AP bin. **g**,**h**, Transcription rate R (**g**) and initiation rate K (**h**) as a function of P_{ON}, for all time points and positions, demonstrating a massive data collapse, suggesting that P_{ON} is the central regulatory parameter for transcriptional bursting. **i**, Control parameters P_{ON} and K as a function of mean transcription rate R in log space. Given that $\log R = \log K + \log P_{ON}$ by construction, changes in P_{ON} determine changes in R below the dashed line ($R \sim 8.5$ mRNA min^{-1}, corresponding to $P_{ON} = 0.75$).

as evident by an overall median error of 10%. Finally, we evaluated the impact of our detection window and threshold on burst characterization and confirmed that our chosen detection parameters minimize errors (Supplementary Fig. 1h,i).

The next goal of our analysis is to elucidate how the consecutive switches between ON and OFF periods quantitatively govern the transcription rate, R. Specifically, the mean transcription rate at time t, denoted $R(t)$, can be decomposed into two distinct parameters: the

https://doi.org/10.1038/s41594-025-01615-4

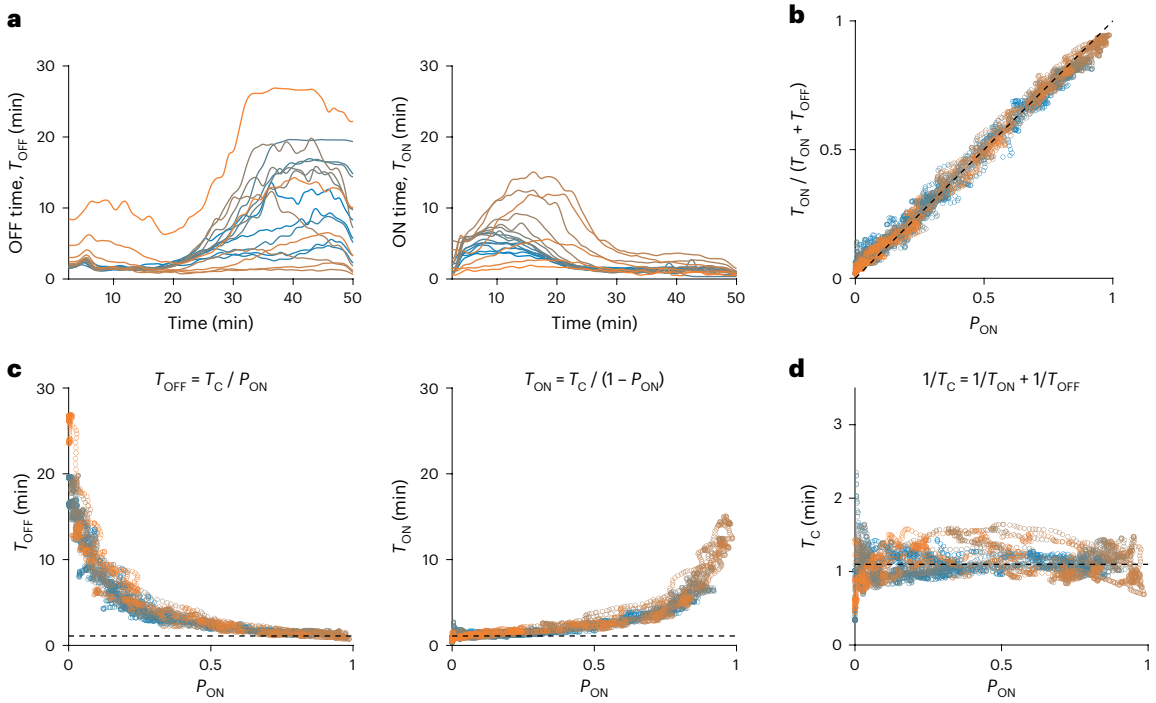

Fig. 3 | Characteristic ON and OFF periods underlie each allele-ON probability. **a**, *Hb* mean OFF time (T_{OFF}) and mean ON time (T_{ON}) as a function of time in NC14 (color encodes AP position). T_{OFF} and T_{ON} are obtained by the weighted average of the ON and OFF periods over all nuclei at the same AP position (see Fig. 2c and Methods). The weights are given by the inverse of the number of time points within each period. **b**, The ratio of T_{ON} over the sum of T_{ON} and T_{OFF} versus ON probability (P_{ON}) for all positions and time points past the 7.5 min mark in **a**. Near steady state, both quantities are expected to be equal after initial transient (see Extended Data Fig. 6l,m). Thus, temporal changes in transcriptional parameters must be slow enough to allow relaxation. **c**, Mean T_{OFF} and T_{ON} as a function of P_{ON} for all positions and time points past the 7.5 min mark in **a**. Dotted line corresponds to mean $T_C = 1.1 \pm 0.2$ in **d**, which sets a lower bound on possible T_{OFF} and T_{ON} values. **d**, Effective switching correlation time T_C (defined as: $1/T_C = 1/T_{ON} + 1/T_{OFF}$) as a function of P_{ON}, computed using data points in **a**. T_C is mostly conserved across time points and position, and is independent of P_{ON}.

instantaneous probability of an allele being in the ON state $P_{ON}(t)$, representing the fraction of ON alleles at time t, and the mean initiation rate, $K(t)$, for ON alleles. The variation in R could arise from changes in either K, P_{ON} or both.

Starting with the gene *hb*, we estimate the time-dependent parameters $R(t)$ and $P_{ON}(t)$ for each anterior–posterior bin. To obtain $R(t)$, we calculate the average of ~250 single-allele instantaneous transcription rates (Fig. 2b). Concurrently, we determine $P_{ON}(t)$ by quantifying the fraction of alleles in the ON state at each time point (Fig. 2c). To compute $K(t)$, we average initiation events restricted to the ON state. By repeating this procedure for all anterior–posterior positions, we reveal the spatiotemporal variations in P_{ON} and K (Fig. 2d–f).

We find that all three parameters vary significantly across space and time (Fig. 2d–f). As expected, we observe the interdependence $R = K \times P_{ON}$ (Extended Data Fig. 6a). However, our analysis reveals that changes in R are primarily governed by variations in P_{ON}, whereas K has a more moderate and less predictive role (Fig. 2g–i and Extended Data Fig. 6d). On average, K displays a threefold change in dynamic range, which is modest compared to R spanning 0 to 15 mRNA min^{-1} (Fig. 2g,h). This variation in K is largely attributable to the presence of two optically unresolved sister chromatids[35] and a modest time dependence of K across nuclear cycles, as we further discuss below (Extended Data Fig. 6e–j and Methods). These findings suggest that the transcriptional activity of *hb* is predominantly controlled by the probability of an allele being in the ON state, while transcription initiation occurs at a largely constant rate once the allele is ON.

Characteristic ON and OFF periods per ON probability

Any given ON probability can result from various combinations of mean ON and OFF periods, denoted as T_{ON} and T_{OFF}. Given that $P_{ON} = T_{ON} / (T_{ON} + T_{OFF})$ near steady state, rescaling both T_{ON} and T_{OFF} can achieve the same P_{ON}. Upon computing the mean ON and OFF periods T_{ON} and T_{OFF} (Extended Data Fig. 6k and Methods), we find that these periods vary substantially across space and time (see Fig. 3a and Extended Data Fig. 6n for full distributions). However, when we plot T_{ON} and T_{OFF} against P_{ON}, we observe that all data points collapse onto two tight, anti-symmetric relationships (Fig. 3b,c). Despite the possibility of multiple combinations of T_{ON} and T_{OFF} for any given P_{ON}, these relationships consistently associate each P_{ON} value with a unique pair of T_{ON} and T_{OFF} values, irrespective of spatial position or time. These findings suggest that the dynamic switching between T_{ON} and T_{OFF} may be governed by an additional intrinsic timescale.

The switching dynamics between ON and OFF states are associated with a correlation time, T_C, which determines the time separation required for the transcription rate of a single allele to become uncorrelated. T_C can be computed directly from the mean ON and OFF times using the equation $1/T_C = 1/T_{ON} + 1/T_{OFF}$ (Fig. 3d). For *hb*, we find that T_C is confined around 1.1 ± 0.2 min across all positions and time points and appears to be independent of P_{ON}.

Given that T_{ON} and T_{OFF} can be expressed as functions of P_{ON} and T_C, namely $T_{ON} = T_C / (1 - P_{ON})$ and $T_{OFF} = T_C / P_{ON}$ (Fig. 3c), the value of T_C corresponds to the lower limit of T_{ON} and T_{OFF} (when P_{ON} approaches one or zero, respectively). We indeed find a similar minimal value for the mean ON and OFF periods on the order of 1–1.5 min, which is larger than the minimal ON and OFF period we can reliably detect (that is, ~30 s and ~10 s, respectively, with an upper bound of ~40 min set by nuclear cycle length; Supplementary Fig. 1f,g and Methods).

Furthermore, the constancy of T_C effectively links the mean ON and OFF times. This provides a mathematical explanation for the tight anti-symmetric relationships between T_{ON}, T_{OFF} and P_{ON} (Fig. 3c). Thus, not only does P_{ON} govern the mean transcription rate R, it also divulges information about the entire transcriptional bursting dynamics, with

https://doi.org/10.1038/s41594-025-01615-4

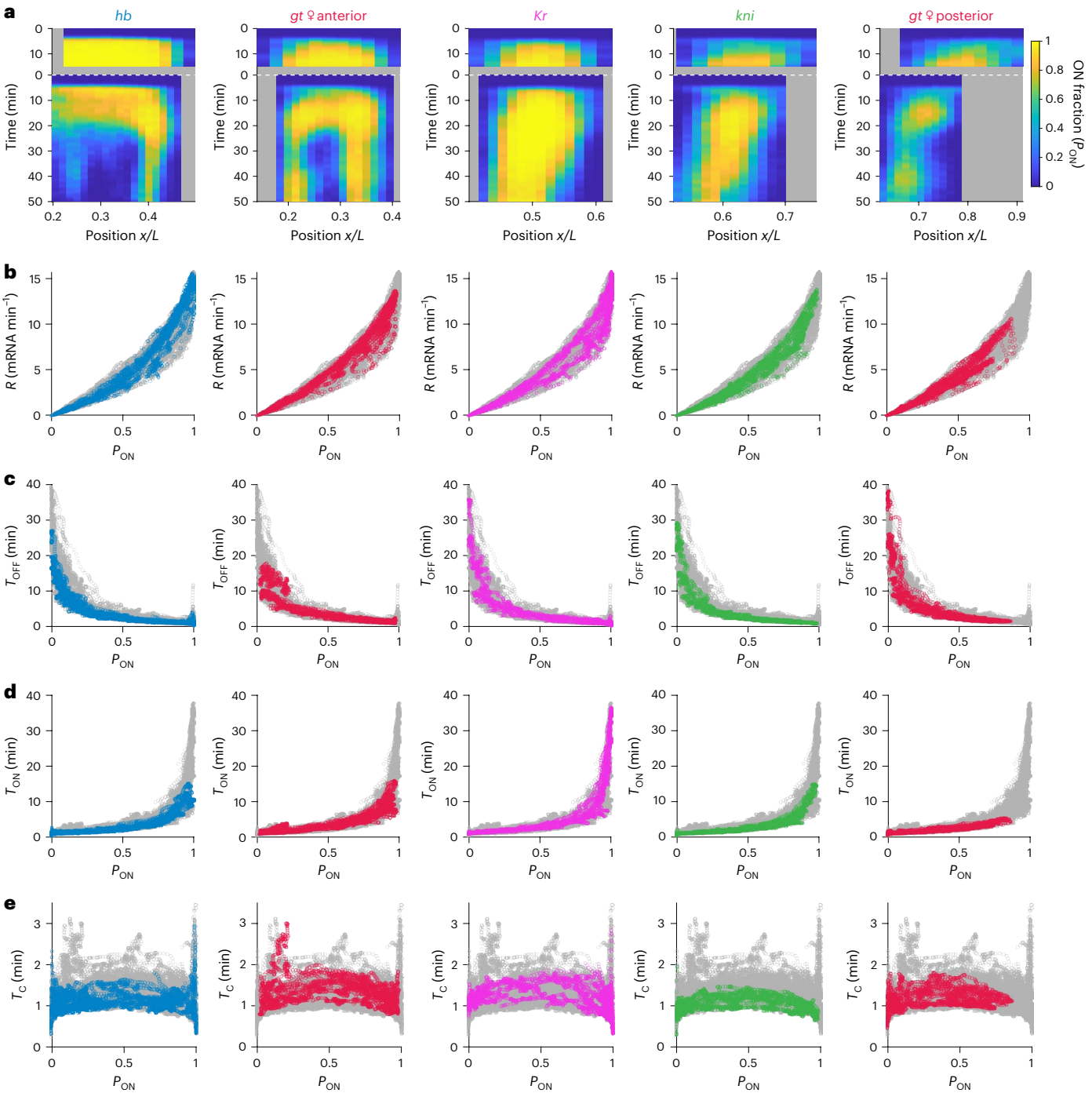

Fig. 4 | Transcription parameters collapse for all gap genes. a, Kymographs of P_{ON} for all gap genes (*hb*, *gt* anterior region, *Kr*, *kni* and *gt* posterior region) as a function of position and time for NC13 and NC14. The spatiotemporal transcriptional pattern of the gap genes arises from a complex regulation of P_{ON} (color map). **b**–**e**, Transcription parameters collapse for all gap genes across time and position. Transcription rate R (**b**), mean OFF time T_{OFF} (**c**), ON time T_{ON} (**d**) and switching correlation time T_C (**e**) as a function of P_{ON}. Colored data points represent individual gap genes (same color code as in **a**; see Extended Data Fig. 7a,b for *gt* male data). Each panel shows all the remaining genes in gray.

a characteristic combination of ON and OFF periods associated with any P_{ON} value.

Common bursting relationships underlie gap gene regulation

The gap genes differ in the composition, number and arrangement of their *cis*-regulatory elements (Extended Data Fig. 1a), resulting in distinct regulatory binding events[36]. Consequently, each gene displays unique spatiotemporal transcriptional activities (Fig. 1c and Video 5). Despite these differences, we find that the relationships governing bursting parameters for *hb* appear to generalize to other gap genes.

When we applied our burst-calling procedure (Fig. 2a) to the transcription time traces of other gap genes (*gt*, *Kr* and *kni*), we obtained distinct spatiotemporal P_{ON} profiles (Fig. 4a and Extended Data Fig. 7a) that closely mirrored the gene-specific transcription rates R. Indeed, all genes exhibit nearly identical relationships between R and P_{ON} (Fig. 4b) and between K and P_{ON} (Extended Data Fig. 7c), affirming that

P_{ON} is the predominant factor governing transcriptional activity across time, space and genes.

The genes exhibit similar T_{OFF}-to-P_{ON} and T_{ON}-to-P_{ON} relationships (Fig. 4c,d). This means that for different genes displaying a specific P_{ON} value—potentially at different spatiotemporal coordinates—the underlying T_{ON} and T_{OFF} periods are largely identical. This finding can be traced back to the conservation of the switching correlation time T_C across all positions, times and genes (Fig. 4e). The average T_C value (1.25 ± 0.37 min) aligns closely with the timescale predicted by the autocorrelation analysis (Fig. 1g). Importantly, the convergence of these bursting relationships among gap genes is not an artifact of our method, as this approach can reliably estimate T_C from 0.5 min to 10 min (Supplementary Fig. 1f,g).

Moreover, the common bursting relationships apply not only across genes but also across distinct spatiotemporal activity domains of a single gene, which can be driven by distinct enhancers[37,38]. This is evident in the large but distinct anterior and posterior domains of the gene *gt* (Fig. 4a and Extended Data Fig. 7a). The use of similar bursting parameters across distinct spatial patterns of a single gene was proposed in a study of a reporter construct of the gene *eve*[39,40].

Pooling the parameters derived from all genes, times and locations—comprising over 3.3×10^4 parameter estimates—highlights the limited subset of the parameter space that is used and underscores the stringent quantitative relationships emerging from our dataset (Fig. 5a–c). When we divide the data into three developmental time windows, these relationships become even more tight, suggesting a modest developmental time dependence (Extended Data Fig. 8a). Notably, the relationships obtained within the first developmental window (spanning NC13 and early NC14) show a twofold improvement in precision compared to our sparse estimates using fixed measurements in NC13 (ref. 23) (Extended Data Fig. 8b).

The relationships obtained are further simplified when we consider that our measurements reflect effective allele rates[16,21,34]. By using the data to gauge the correlation between the unresolved sister chromatids, we can compute single gene copy parameters (Extended Data Fig. 8c and Supplementary Figs. 3 and 4). Specifically, we find that a two-state model, with largely independent or weakly correlated sister chromatids, recapitulates key statistical properties of the data (Supplementary Fig. 3). This model allows us to estimate the mean initiation rate for a single active copy at 6.4 ± 1.3 mRNA min^{-1} and recover a mean Pol II spacing of 299 ± 99 bp. This is consistent with the classic Miller spreads with average Pol II spacing of 330 ± 180 bp[41]. Furthermore, when we convert our entire set of single allele parameters into their single gene copy equivalent, the largely conserved K and the almost linear relationship between R to P_{ON} become even more evident (Extended Data Fig. 8c and Supplementary Fig. 4). Thus, our analysis shows that across all data points, the mean transcription rate R is primarily governed by P_{ON}, with only limited modulation of K.

The near-constant switching correlation time T_C observed across the pooled dataset is associated with an apparent inverse proportionality between T_{ON} and T_{OFF}, with a predominant modulation of one of these two parameters when P_{ON} changes. Although lowly transcribing alleles (as characterized by P_{ON}) tend to achieve higher expression levels mainly by reducing T_{OFF}, medium-to-high-transcribing alleles are predominantly tuned by extending T_{ON} (Fig. 5d). This observation means that changes in burst frequency ($F = 1/(T_{ON} + T_{OFF})$) govern tuning of the transcriptional activity of low-transcribing alleles, while changes in burst size ($B = K \times T_{ON}$) exert greater influence on the tuning of medium-to-high-transcribing alleles (Fig. 5c,e).

The association between gene activity level and bursting parameters holds across genes, spatial locations and time points (Fig. 5 and Extended Data Figs. 7 and 8), indicating its relevance across diverse regulatory landscapes.

Bursting relationships predict *cis* and *trans* perturbations

A multitude of regulatory determinants, including *cis*-regulatory elements like enhancers and *trans* factors such as transcription factor repressors, collectively shape transcriptional outcomes. It is commonly assumed that distinct regulatory mechanisms directly influence specific bursting parameters. Thus, we sought to perturb various regulatory determinants to assess whether they produce distinct effects on bursting dynamics or follow the relationships identified from wild-type measurements.

Upon endogenous deletion of the distal enhancer of *hb*, we observe significant alterations in transcriptional activity (Fig. 6a,b and Supplementary Video 7), including increased or decreased activity, at different times and locations along the anterior–posterior axis, consistent with previous findings[42]. However, we find that bursting dynamics in this mutant still adhere to the wild-type relationships. Specifically, transcription rates across spatiotemporal coordinates are again governed by P_{ON}, the stringent relationships between T_{ON}, T_{OFF} and P_{ON} hold and the switching correlation time T_C remains broadly conserved around 0.9 ± 0.2 min (Fig. 6c Extended Data Fig. 9g–j).

Two additional perturbations further confirmed these findings. Deleting the distal enhancer of *kni* results in a significant reduction in *kni* activity (Extended Data Fig. 9a,b and Supplementary Video 8). Although the mutant exhibits a narrower dynamic range of activity, we observe a similar data collapse within this reduced range (Extended Data Fig. 9c,g–j). Next, we explored the effect of a *trans* perturbation by measuring *kni* activity in embryos with a *hb* null background (Extended Data Fig. 9d,e and Supplementary Video 9). This *trans* perturbation significantly alters *kni* activity, consistent with earlier studies[43,44] (Extended Data Fig. 9f). However, the underlying bursting dynamics again collapse onto the same bursting relationships (Fig. 6d and Extended Data Fig. 9g–j).

The consistency of P_{ON}-to-T_{ON} and P_{ON}-to-T_{OFF} relationships in wild-type and mutants suggests that we can predict how ON and OFF periods change upon a perturbation. Performing such a prediction relies solely on how the activity level, captured by P_{ON}, changed. Notably, for each type of perturbation, we predict instances of predominant T_{ON} and instances of predominant T_{OFF} modulation at different spatiotemporal coordinates (Fig. 6e). Comparing predictions based on the wild-type-derived relationships with the directly measured T_{ON} and T_{OFF} from the mutant, we find agreement as to which parameter was primarily altered in more than ~86% of cases for all spatiotemporal coordinates (Fig. 6e and Extended Data Fig. 9k,m,o). Additionally, similar successful predictions are achieved when assessing the change in transcriptional activity in terms of altered burst size versus burst frequency (Fig. 6f and Extended Data Fig. 9l,n,p). These findings challenge previous intuitions linking perturbations of specific regulatory elements or mechanisms to changes in a particular bursting parameter. Instead, these findings suggest the predictive power of P_{ON}, a proxy of the transcription activity, across different perturbations.

To further explore the generality of these observations, we examined data from two previous studies in the early fly embryo. One focused on the transcriptional effect of BMP signaling, a dorsoventral morphogen[16]. Transcription of a BMP target gene, u-shaped (*ush*), was measured across different dorsoventral positions and under ectopic signaling. A second study used synthetic reporter constructs to examine the transcriptional effect of two core promoter motifs (TATA box and Initiator)[21]. These studies pointed to the modulation of distinct bursting parameters, and although the analyzed genes and perturbed regulatory determinants differ from those we measured, we found that the datasets collapse onto our identified bursting relationships (Fig. 6g).

As suggested in these studies, the first dataset shows predominantly T_{OFF} modulation, while the latter study has primarily T_{ON} changes. Intriguingly, when plotted in the context of the full spectrum of P_{ON}

https://doi.org/10.1038/s41594-025-01615-4

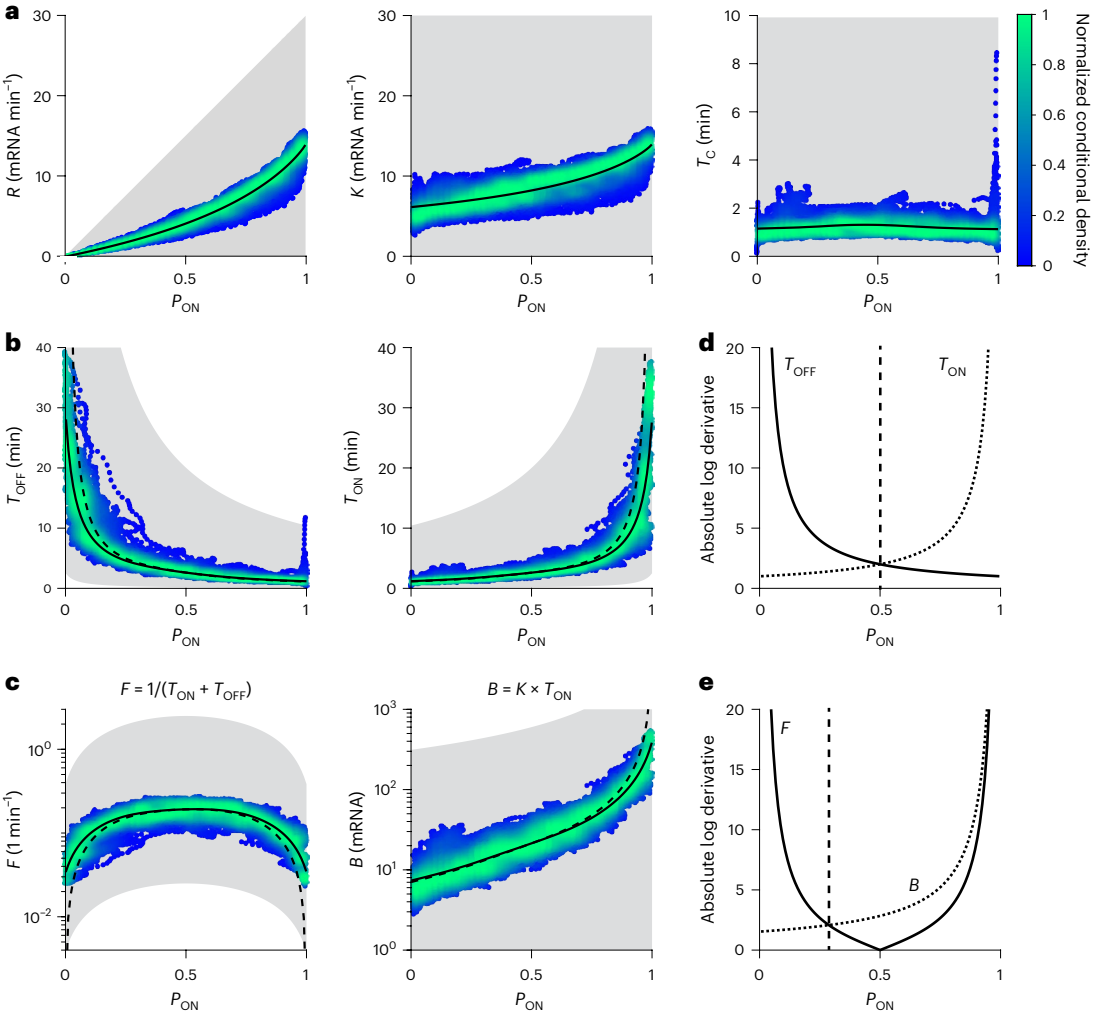

Fig. 5 | Bursting parameters sample a restricted space and follow tight relationships. a–**c**, Global scatter and density (color) of transcription parameter estimates for all gap genes across space and time as a function of P_{ON}, normalized by the maximum conditional density with respect to P_{ON}. Potentially accessible space (gray shade) for plausible ranges of K (0.1–30 mRNA min^{-1}) and T_C (0.1–10 min). **a**, P_{ON} almost fully determines R, as K is mostly constant. **b**, P_{ON} sets the combinations of T_{OFF} and T_{ON} as T_C is constant. The dashed lines are the two-state model predictions based on T_C, and the solid lines take the finite recording length into account (Extended Data Fig. 7d). **c**, Decomposition of R in terms of burst frequency, F, and burst size, B (with $R = F \times B$ and definition on top). P_{ON} determines both F and B, as K and T_C are mostly constant. **d**, Absolute derivatives of log T_{OFF} and log T_{ON} with respect to P_{ON}. Log decomposition is convenient as the dominant sources of P_{ON} variation become approximately additive (as $\log P_{ON} \approx \log \frac{P_{ON}}{1-P_{ON}} = \log T_{ON} - \log T_{OFF}$). For $P_{ON} < 1/2$, changes are primarily driven by T_{OFF}; for $P_{ON} > 1/2$, by T_{ON}. **e**, Absolute derivatives of log F and log B with respect to P_{ON}. Similar to **d**, dominant sources of R variation are additive ($\log R = \log F + \log B$). For $P_{ON} < 1/3$, changes are primarily driven by F; for $P_{ON} > 1/3$, by B.

values captured by our measurements, the two independent datasets cluster in disjoint halves (Fig. 6g). Our analysis raises the possibility that the predominantly changed parameter (T_{OFF} versus T_{ON}) might not be inherent to the examined regulatory manipulation (for example, input transcription factor concentrations or core promoter elements) but rather a consequence of the expression range (the P_{ON} regime) of these genes.

Data across organisms adheres to bursting relationships

The conserved nature of the transcription machinery and regulatory mechanisms across eukaryotes suggests that fundamental properties, probably reflecting molecular constraints, apply to numerous systems[45]. However, technical and biological factors currently hinder the ability to perform direct measurements of bursting dynamics and quantitatively compare parameter values or dependencies across diverse settings. For example, our analysis above highlights the necessity of a large dynamic range of gene activity to reveal underlying relationships. Yet a large dynamic range is not readily observed in many setups. Using absolute units (for example, calibrating arbitrary fluorescent units to mRNA counts) is crucial for estimating measurement sensitivity and facilitating comparisons across genes, perturbations and systems. Additionally, an analysis that decouples the contribution of different biological steps to the measured signal (for example, transcription initiation, elongation and mRNA half lives) is essential. These considerations guided our re-examination of data in yeast and mammalian cells.

To facilitate comparison, we computed the equivalent single gene copy parameters for all the fly data, as discussed above (Extended Data Fig. 8c, Supplementary Fig. 4 and Methods). We examined bursting parameters derived from extensive perturbations of a yeast gene[19] and found strong agreement with our observations from the early fly embryo (Fig. 7a). Although the yeast data points span a relatively small range of bursting parameters compared to the developmentally regulated *Drosophila* genes, they are consistent with the T_{ON}-to-P_{ON} and T_{OFF}-to-P_{ON} relationships and show a highly constrained T_C value of 1.1 ± 0.1 min, within our observed range.

https://doi.org/10.1038/s41594-025-01615-4

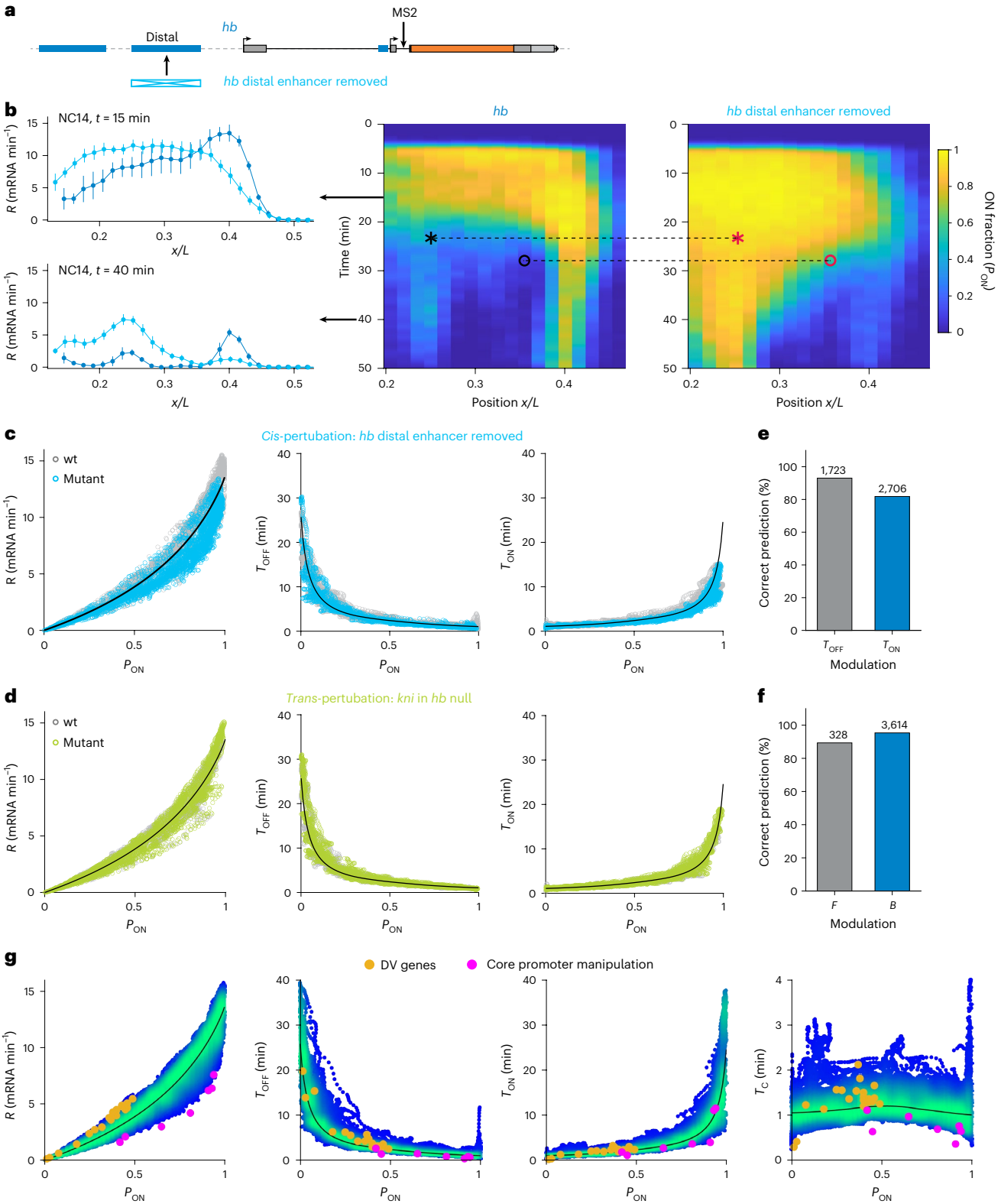

Fig. 6 | Effect of *cis* and *trans* perturbations on ON and OFF times. a, Distal *hb* enhancer removal from the fly line carrying MS2 stem-loops in the endogenous *hb* locus. **b**, Quantification of *hb* wild-type (wt) and mutant phenotypes. Both transcription rate R (left) and P_{ON} (right) levels display significantly different expression patterns for the enhancer deletion mutant. Black arrows indicate the time points (15 and 40 min into NC14) in the kymograph at which rate profiles are depicted. 'o' and '*' mark two bins with predominant T_{OFF} modulation and predominant T_{ON} modulation, respectively. Error bars are 1 s.d. across embryo means. **c**, Transcription parameters for *hb* enhancer deletion (cyan) collapse on corresponding wild-type parameters (gray). **d**, Transcription parameters for *kni* (green) in a *hb* null background (that is, a *trans* mutation; Extended Data Fig. 9d,e) collapse on corresponding wild-type parameters (gray). Solid black lines in **c** and **d** correspond to the endogenous bursting relationships from Fig. 5. **e**,**f** Verification of predicted changes in T_{OFF} and T_{ON} (**e**) and changes in burst size B and frequency F (**f**) for all wild-type and mutant P_{ON} pairs (two example pairs shown in **a** for *hb*). For most pairs (>85%), the prediction is correct (see Extended Data Fig. 9k–p). **g**, Transcription parameters computed from two other *Drosophila* studies (yellow circles[16] and pink circles[21], respectively) are consistent with the gap genes relationships (black lines; data density color-coded as in Fig. 5). DV, dorsoventral.

https://doi.org/10.1038/s41594-025-01615-4

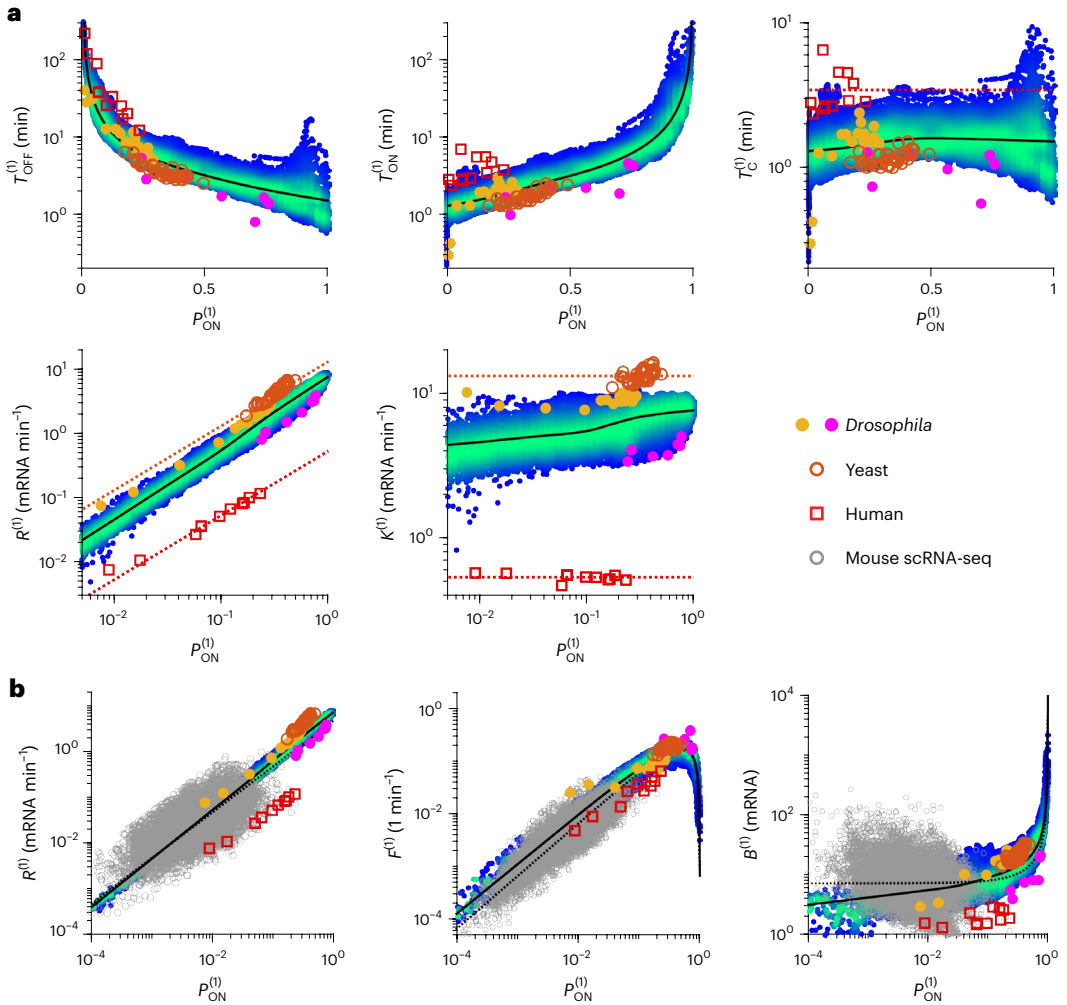

Fig. 7 | Generality of bursting relationships. a, Scatter plots of the transcription parameters for a single gene copy versus P_{ON} (color-coded as in Fig. 5). As in Fig. 6g, transcription parameters computed from two other *Drosophila* studies (yellow circles[16] and pink circles[21]) are included. Transcription parameters resulting from multiple perturbations performed on the yeast *GAL10* gene (orange circles[19]) also closely follow our relationships (black lines), suggesting that these may apply to other species in addition to *Drosophila*. Transcription parameters estimated using our deconvolution approach on 11 human genes (red squares[9,51]) further highlight the constant nature of T_C and K (see Methods). **b**, Transcription rate R, burst frequency F and burst size B for a single gene copy versus P_{ON}. Transcription parameters estimated from allelic scRNA-seq in mouse cells (gray circles[22]) are mostly consistent with our relationships (black lines). Black dotted lines correspond to expected relationships in scRNA-seq data assuming constant K and T_C (see Supplementary Fig. 5c).

Two high-throughput studies conducted in mammalian systems used vastly different approaches—randomly integrated GFP reporters and single-cell RNA sequencing (scRNA-seq)—but both indicate trends that align with our elucidated bursting relationships[22,46,47]. Extrinsic noise related to cell size and the cell cycle[47] (which is largely mitigated in the highly synchronized early fly embryo), sampling issues like the low mRNA capture rate in scRNA-seq and long mRNA dwell times (on the order of hours)[48], confound quantitative comparisons of bursting parameters across studies[49,50]. However, although one of the studies[46] used a GFP reporter with a 2 h half-life randomly integrated into a human cell line, their analysis of fluorescent protein noise suggested modulation of burst frequency in loci with low GFP activity and modulation of burst size in loci with high GFP activity. This is consistent with what we now observe through an endogenous transcriptional readout.

To extract bursting parameters from the study of the mouse cells' scRNA-seq[22], we fitted the steady-state mRNA distributions as in the original study, with an additional weak prior on T_C. The resulting fits are as good as the original ones (marginal loss in likelihood; see Methods) and provide parameter estimates with plausible physical scales (Supplementary Fig. 5a,b). We further corrected for cell size variability and low mRNA capture rate in the data[49], with minimal impact on the estimated parameter trends (Fig. 7b and Supplementary Fig. 5c,d). The inferred parameters from scRNA-seq are overall consistent with our elucidated bursting relationships. The analysis highlights the potential of using parameters derived from live imaging to interpret scRNA-seq data in terms of physical kinetic rates, which can be linked to underlying molecular events.

Owing to the inherent challenges of extracting bursting parameters from protein levels or snapshot scRNA-seq data, we sought live transcription measurements of mammalian genes. We reanalyzed time traces from 11 endogenous human genes imaged with the MS2 system in cell lines[9,51]. Our goal was to extract a promoter ON time that captures initiation, rather than the previously reported ON time encompassing both initiation and mRNA dwell time.

We calibrated the signal in absolute units using smFISH measurements of nascent mRNA from one of these genes (*TFF1*)[51] and performed a fluctuation analysis to assess measurement noise and mean mRNA dwell time. After deconvolving initiation events, we estimated bursting parameters for these genes, acknowledging longer mRNA dwell times (6–16 min vs 1–2 min in flies), lower temporal resolution (100 s) and measurement noise as contributors to uncertainties in these estimates (see Methods). The resulting parameters closely match those obtained

https://doi.org/10.1038/s41594-025-01615-4

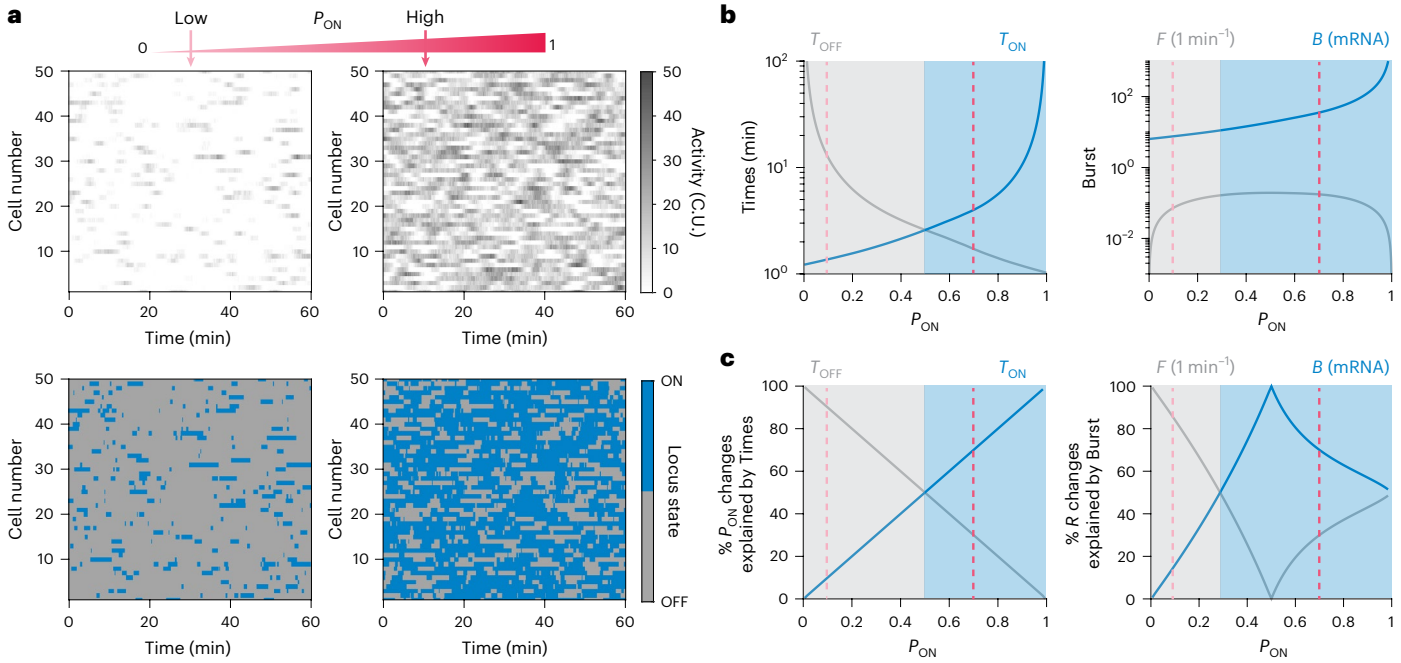

Fig. 8 | Decoding bursting regimes from gene expression. a, Heatmaps of simulated single allele activity (top) and of corresponding ON–OFF gene state (bottom) for a low and high P_{ON} regime, as predicted from our bursting relationships (see **b**). **b**, The bursting relationships extracted from our data characterize single-allele bursting dynamics, as shown in **a**. **c**, Fractional changes in activity explained by T_{OFF} and T_{ON} (left) and are explained by burst frequency F and size B (right). For low P_{ON} (<0.5), changes in activity are predominantly dictated by changes in T_{OFF}, and for high P_{ON} (>0.5), by changes in T_{ON}. Similarly, for low P_{ON} (<1/3), changes in activity are mainly dictated by changes in F, and for high P_{ON} (>1/3), by changes in B.

from the fluctuation analysis performed in the original study on the gene *TFF1* (ref. 51). Across genes, we find that both the initiation rate K and the switching correlation time T_C are mainly constant, around $K = 0.54 \pm 0.02$ mRNA min^{-1} and $T_C = 3.2 \pm 0.8$ min, respectively (Fig. 7a). Although absolute values for K, and to a lesser extent T_C, appear to differ from fly genes (12-fold and twofold difference, respectively), the predictive power of P_{ON} is preserved, and the human genes follow very similar relationships.

Although the initiation rate K appears largely conserved across genes and conditions within a given organism, we observe notable differences between the three species we probed (yeast $K = 13.2 \pm 1.3$, fly $K = 6.2 \pm 1.8$ and human $K = 0.54 \pm 0.02$; Fig. 7a). In addition to the reduced K, mouse and human genes use a lower P_{ON} range overall[6,9,22,51], which leads to smaller transcription rates (Fig. 7b). These differences may reflect species-specific metabolic variations[52,53]. Despite these differences in K and P_{ON}, the T_C values are strikingly similar across species. Most importantly, the relationships between bursting parameters remain consistent across these datasets, possibly reflecting conserved underlying mechanisms.

Discussion

In this study, we developed a method to quantify real-time transcriptional bursting at single alleles in developing early *Drosophila* embryos. The broad range of transcriptional activities in this system enabled us to uncover fundamental relationships governing bursting dynamics. Specifically, we found a highly restrictive regime characterized by tight, asymmetric relationships between T_{OFF}, T_{ON} and P_{ON}, anchored by a relatively low and largely invariant timescale, T_C. Importantly, we show that these relationships generalize, as they also align with data from yeast and mammalian cells[19,22,51], pointing to conserved underlying mechanisms.

Low-activity alleles exhibit longer OFF times and shorter ON times, while high-activity alleles ($P_{ON} > 0.5$) show the opposite trend (Fig. 8a,b). Changes in activity level are primarily driven by shortening OFF periods at low activity and by prolonging ON periods at mid-to-high activity (Fig. 8c, left). Correspondingly, transcriptional tuning at the extremes of activity—very low or very high—is associated with larger changes in burst frequency ($F = 1/(T_{ON} + T_{OFF})$). However, although changes in burst frequency dominate at low activity, changes in burst size ($B = K \times T_{ON}$) become the primary mode of modulation at mid-to-high activity (Fig. 8c, right). This observation holds even when using an alternative definition of burst frequency, $F = 1/T_{OFF}$ (Supplementary Fig. 5d), commonly applied when $T_{OFF} > T_{ON}$[22,46,54]. This trend echoes measurements from GFP reporters in human cells, where low-GFP-expressing versus high-GFP-expressing loci predominantly modulate burst frequency or size, respectively[46], suggesting the potential generality of this association between an activity range and a predominant bursting parameter modulated.

Our discovery of tight relationships between transcriptional bursting parameters does not depend on fitting specific mechanistic models. Instead, we directly identify ON and OFF periods from single-allele initiation events, which requires careful signal quantification (Extended Data Fig. 1). These relationships are further supported by single-allele time trace autocorrelation analysis (Fig. 1g and Extended Data Fig. 5d), which does not rely on ON–OFF calling. By avoiding model-specific assumptions, our analysis remains broadly applicable across diverse transcriptional models (Supplementary Fig. 1c–f).

Our approach complements studies that involve fitting detailed mechanistic models[9,12,17,21,32,33]. Although mechanistic modeling is valuable for testing a specific hypothesis, our generic analysis aims to map the space of used bursting parameters and uncover regularities. These regularities, in turn, can guide the design of plausible models linking molecular processes to bursting dynamics. Indeed, the relationships we identify impose strong constraints on the kinetic parameters of mechanistically detailed transcription models (Supplementary Fig. 3). For instance, any multi-state model[9,12,17,21,32,33] that seeks to explain the data must reproduce the observed effective mean ON and OFF periods and adhere to the relationships we have elucidated.

The observed relationships do not trivially map to commonly invoked molecular processes shaping transcriptional dynamics. This suggests novel mechanistic constraints and underscores the need to

uncover their molecular underpinnings. Mathematically, the observed regime can be described in two equivalent ways: either as governed by P_{ON} (with mean activity proportional to P_{ON}) and a largely constant and low value of T_C; or as regulation through both T_{ON} and T_{OFF}, where $1/T_{ON} + 1/T_{OFF}$ is largely constant and mean activity is proportional to $T_{ON}/(T_{ON} + T_{OFF})$. Mechanistically, one of these descriptions might better capture the underlying molecular events.

Several key questions emerge from this framework: specifically, whether there are molecular mechanisms that enable diverse regulatory processes to converge on modulating P_{ON} as a central parameter; whether specific regulatory determinants dominate in distinct regions of the parameter space, such as lower versus higher P_{ON}; whether there is dedicated molecular tuning of T_{ON} or T_{OFF} and how the observed constancy of $1/T_{ON} + 1/T_{OFF}$ ($= 1/T_C$) is achieved; and whether there could be a direct molecular implementation to this constancy, or to the low value of T_C itself.

The measured value of T_C ~ 1 min is reliably above our detection limit (Methods) yet remarkably small given the theoretically accessible parameter space (Fig. 5a). This value also corresponds to the shortest ON and OFF durations we observe, occurring at P_{ON} values close to 0 or 1, respectively, as defined by $T_{ON} = T_C/(1 - P_{ON})$ and $T_{OFF} = T_C/P_{ON}$. Notably, it is non-trivial that these periods display similar minimal durations, as distinct molecular events might govern the ON and OFF states.

The constancy of T_C across genes, perturbations and organisms, which corresponds to the tight linkage between ON and OFF periods, raises intriguing possibilities. It may stem from aspects of the transcriptional environment that have only recently gained appreciation, such as the nuclear architecture or the assembly and disassembly of transcription machinery components[55–60].

Intriguingly, the identified bursting relationships align with a simple ON–OFF bursting regime in which periods have a lower limit, and any P_{ON} is encoded with the shortest possible combination of ON and OFF durations, effectively minimizing $T_{ON} + T_{OFF}$ (or maximizing burst frequency; Extended Data Fig. 10). These assumptions yield a narrow parameter space, as we observe asymmetric relationships between P_{ON} and T_{OFF} or T_{ON} and a consistently low T_C across the full P_{ON} range. Thus, this regime captures key features of the data and offers a different way of thinking about the mechanisms involved. Such a regime may offer functional advantages to developmental regulation by enabling fine-tuning of gene expression with minimal resource expenditure.

A conserved low T_C also corresponds to a reduced noise in gene expression as bursts can be effectively buffered by longer mRNA lifetimes[23] (see Methods). Moreover, transcription remains highly responsive, with gene expression outcomes rapidly adjusting to changes in transcription factor inputs (Extended Data Fig. 6l,m). These features suggest that such regimes support both stability and adaptability in transcriptional control. Thus, similar to other emerging organizing principles[61–65], the relationships uncovered here point to functionality encoded by complex processes and provide a foundation for future investigations to explore the underlying molecular mechanisms.

Online content

Any methods, additional references, Nature Portfolio reporting summaries, source data, extended data, supplementary information, acknowledgements, peer review information; details of author contributions and competing interests; and statements of data and code availability are available at https://doi.org/10.1038/s41594-025-01615-4.

References

1. Lelli, K. M., Slattery, M. & Mann, R. S. Disentangling the many layers of eukaryotic transcriptional regulation. *Annu. Rev. Genet.* **46**, 43–68 (2012).
2. Cramer, P. Eukaryotic transcription turns 50. *Cell* **179**, 808–812 (2019).
3. Raj, A., Peskin, C. S., Tranchina, D., Vargas, D. Y. & Tyagi, S. Stochastic mRNA synthesis in mammalian cells. *PLoS Biol.* **4**, 1707–1719 (2006).
4. Chubb, J. R., Trcek, T., Shenoy, S. M. & Singer, R. H. Transcriptional pulsing of a developmental gene. *Curr. Biol.* **16**, 1018–1025 (2006).
5. Zenklusen, D., Larson, D. R. & Singer, R. H. Single-RNA counting reveals alternative modes of gene expression in yeast. *Nat. Struct. Mol. Biol.* **15**, 1263–1271 (2008).
6. Suter, D. M. et al. Mammalian genes are transcribed with widely different bursting kinetics. *Science* **332**, 472–474 (2011).
7. Bothma, J. P. et al. Dynamic regulation of *eve* stripe 2 expression reveals transcriptional bursts in living *Drosophila* embryos. *Proc. Natl Acad. Sci. USA* **111**, 10598–10603 (2014).
8. Tantale, K. et al. A single-molecule view of transcription reveals convoys of RNA polymerases and multi-scale bursting. *Nat. Commun.* **7**, 12248 (2016).
9. Wan, Y. et al. Dynamic imaging of nascent RNA reveals general principles of transcription dynamics and stochastic splice site selection. *Cell* **184**, 2878–2895.e20 (2021).
10. Senecal, A. et al. Transcription factors modulate c-Fos transcriptional bursts. *Cell Rep.* **8**, 75–83 (2014).
11. Bartman, C. R., Hsu, S. C., Hsiung, C. C. S., Raj, A. & Blobel, G. A. Enhancer regulation of transcriptional bursting parameters revealed by forced chromatin looping. *Mol. Cell* **62**, 237–247 (2016).
12. Li, C., Cesbron, F., Oehler, M., Brunner, M. & Höfer, T. Frequency modulation of transcriptional bursting enables sensitive and rapid gene regulation. *Cell Syst.* **6**, 409–423.e11 (2018).
13. Nicolas, D., Zoller, B., Suter, D. M. & Naef, F. Modulation of transcriptional burst frequency by histone acetylation. *Proc. Natl Acad. Sci. USA* **115**, 7153–7158 (2018).
14. Donovan, B. T. et al. Live-cell imaging reveals the interplay between transcription factors, nucleosomes, and bursting. *EMBO J.* **38**, e100809 (2019).
15. Falo-Sanjuan, J., Lammers, N. C., Garcia, H. G. & Bray, S. J. Enhancer priming enables fast and sustained transcriptional responses to notch signaling. *Dev. Cell* **50**, 411–425.e8 (2019).
16. Hoppe, C. et al. Modulation of the promoter activation rate dictates the transcriptional response to graded BMP signaling levels in the *Drosophila* embryo. *Dev. Cell* **54**, 727–741.e7 (2020).
17. Tantale, K. et al. Stochastic pausing at latent HIV-1 promoters generates transcriptional bursting. *Nat. Commun.* **12**, 4503 (2021).
18. Bass, V. L., Wong, V. C., Bullock, M. E., Gaudet, S. & Miller-Jensen, K. TNF stimulation primarily modulates transcriptional burst size of NF-κB-regulated genes. *Mol. Syst. Biol.* **17**, e10127 (2021).
19. Brouwer, I., Kerklingh, E., van Leeuwen, F. & Lnestra, T. L. Dynamic epistasis analysis reveals how chromatin remodeling regulates transcriptional bursting. *Nat. Struct. Mol. Biol.* **30**, 692–702 (2023).
20. Fukaya, T., Lim, B. & Levine, M. Enhancer control of transcriptional bursting. *Cell* **166**, 358–368 (2016).
21. Pimmett, V. L. et al. Quantitative imaging of transcription in living *Drosophila* embryos reveals the impact of core promoter motifs on promoter state dynamics. *Nat. Commun.* **12**, 4504 (2021).
22. Larsson, A. J. M. et al. Genomic encoding of transcriptional burst kinetics. *Nature* **565**, 251–254 (2019).
23. Zoller, B., Little, S. C. & Gregor, T. Diverse spatial expression patterns emerge from unified kinetics of transcriptional bursting. *Cell* **175**, 835–847.e25 (2018).
24. Levo, M. et al. Transcriptional coupling of distant regulatory genes in living embryos. *Nature* **605**, 754–760 (2022).
25. Bertrand, E. et al. Localization of ASH1 mRNA particles in living yeast. *Mol. Cell* **2**, 437–445 (1998).
26. Larson, D. R., Zenklusen, D., Wu, B., Chao, J. A. & Singer, R. H. Real-time observation of transcription initiation and elongation on an endogenous yeast gene. *Science* **332**, 475–478 (2011).

27. Garcia, H. G., Tikhonov, M., Lin, A. & Gregor, T. Quantitative imaging of transcription in living *Drosophila* embryos links polymerase activity to patterning. *Curr. Biol.* **23**, 2140–2145 (2013).
28. Lucas, T. et al. Live imaging of bicoid-dependent transcription in *Drosophila* embryos. *Curr. Biol.* **23**, 2135–2139 (2013).
29. Liu, J. et al. Real-time single-cell characterization of the eukaryotic transcription cycle reveals correlations between RNA initiation, elongation, and cleavage. *PLoS Comput. Biol.* **17**, e1008999 (2021).
30. Dubuis, J. O., Samanta, R. & Gregor, T. Accurate measurements of dynamics and reproducibility in small genetic networks. *Mol. Syst. Biol.* **9**, 639 (2013).
31. Peccoud, J. & Ycart, B. Markovian modeling of gene-product synthesis. *Theor. Popul. Biol.* **48**, 222–234 (1995).
32. Neuert, G. et al. Systematic identification of signal-activated stochastic gene regulation. *Science* **339**, 584–587 (2013).
33. Zoller, B., Nicolas, D., Molina, N. & Naef, F. Structure of silent transcription intervals and noise characteristics of mammalian genes. *Mol. Syst. Biol.* **11**, 823 (2015).
34. Lammers, N. C. et al. Multimodal transcriptional control of pattern formation in embryonic development. *Proc. Natl Acad. Sci. USA* **117**, 836–847 (2020).
35. Hua, B. L. & Orr-Weaver, T. L. DNA replication control during *Drosophila* development: insights into the onset of S phase, replication initiation, and fork progression. *Genetics* **207**, 29–47 (2017).
36. Lagha, M., Bothma, J. P. & Levine, M. Mechanisms of transcriptional precision in animal development. *Trends Genet.* **28**, 409–416 (2012).
37. Schroeder, M. D. et al. Transcriptional control in the segmentation gene network of *Drosophila*. *PLoS Biol.* **2**, E271 (2004).
38. Perry, M. W., Bothma, J. P., Luu, R. D. & Levine, M. Precision of hunchback expression in the *Drosophila* embryo. *Curr. Biol.* **22**, 2247–2252 (2012).
39. Berrocal, A., Lammers, N., Garcia, H. G. & Eisen, M. B. Kinetic sculpting of the seven stripes of the *Drosophila even-skipped* gene. *eLife* **9**, e61635 (2020).
40. Berrocal, A., Lammers, N. C., Garcia, H. G. & Eisen, M. B. Unified bursting strategies in ectopic and endogenous *even-skipped* expression patterns. *eLife* **12**, RP88671 (2023).
41. McKnight, S. L. & Miller, O. L. Post-replicative nonribosomal transcription units in *D. melanogaster* embryos. *Cell* **17**, 551–563 (1979).
42. Fukaya, T. Dynamic regulation of anterior–posterior patterning genes in living *Drosophila* embryos. *Curr. Biol.* **31**, 2227–2236.e6 (2021).
43. Hulskamp, M., Lukowitz, W., Beermann, A., Glaser, G. & Tautz, D. Differential regulation of target genes by different alleles of the segmentation gene hunchback in *Drosophila*. *Genetics* **138**, 125–134 (1994).
44. Haroush, N., Levo, M., Wieschaus, E. F. & Gregor, T. Functional analysis of the *Drosophila* eve locus in response to non-canonical combinations of gap gene expression levels. *Dev. Cell* **58**, 2789–2801.e5 (2023).
45. Sanchez, A. & Golding, I. Genetic determinants and cellular constraints in noisy gene expression. *Science* **342**, 1188–1193 (2013).
46. Dar, R. D. et al. Transcriptional burst frequency and burst size are equally modulated across the human genome. *Proc. Natl Acad. Sci. USA* **109**, 17454–17459 (2012).
47. Berry, S. & Pelkmans, L. Mechanisms of cellular mRNA transcript homeostasis. *Trends Cell Biol.* **32**, 655–668 (2022).
48. Herzog, V. A. et al. Thiol-linked alkylation of RNA to assess expression dynamics. *Nat. Methods* **14**, 1198–1204 (2017).
49. Tang, W., Jørgensen, A. C. S., Marguerat, S., Thomas, P. & Shahrezaei, V. Modelling capture efficiency of single-cell RNA-sequencing data improves inference of transcriptome-wide burst kinetics. *Bioinformatics* **39**, btad395 (2023).
50. Grima, R. & Esmenjaud, P. M. Quantifying and correcting bias in transcriptional parameter inference from single-cell data. *Biophys. J.* **123**, 4–30 (2024).
51. Rodriguez, J. et al. Intrinsic dynamics of a human gene reveal the basis of expression heterogeneity. *Cell* **176**, 213–226. e18 (2019).
52. Rayon, T. et al. Species-specific pace of development is associated with differences in protein stability. *Science* **369**, eaba7667 (2020).
53. Diaz-Cuadros, M. et al. Metabolic regulation of species-specific developmental rates. *Nature* **613**, 550–557 (2023).
54. Meeussen, J. V. W. & Lenstra, T. L. Time will tell: comparing timescales to gain insight into transcriptional bursting. *Trends Genet.* **40**, 160–174 (2024).
55. Tsai, A. et al. Nuclear microenvironments modulate transcription from low-affinity enhancers. *eLife* **6**, e28975 (2017).
56. Cho, W. K. et al. Mediator and RNA polymerase II clusters associate in transcription-dependent condensates. *Science* **361**, 412–415 (2018).
57. Li, J. et al. Single-gene imaging links genome topology, promoter–enhancer communication and transcription control. *Nat. Struct. Mol. Biol.* **27**, 1032–1040 (2020).
58. Henninger, J. E. et al. RNA-mediated feedback control of transcriptional condensates. *Cell* **184**, 207–225.e24 (2021).
59. Nguyen, V. Q. et al. Spatiotemporal coordination of transcription preinitiation complex assembly in live cells. *Mol. Cell* **81**, 3560–3575.e6 (2021).
60. Brückner, D. B., Chen, H., Barinov, L., Zoller, B. & Gregor, T. Stochastic motion and transcriptional dynamics of pairs of distal DNA loci on a compacted chromosome. *Science* **380**, 1357–1362 (2023).
61. Tkačik, G., Callan, C. G. & Bialek, W. Information flow and optimization in transcriptional regulation. *Proc. Natl Acad. Sci. USA* **105**, 12265–12270 (2008).
62. Jones, D. L., Brewster, R. C. & Phillips, R. Promoter architecture dictates cell-to-cell variability in gene expression. *Science* **346**, 1533–1536 (2014).
63. Hausser, J., Mayo, A., Keren, L. & Alon, U. Central dogma rates and the trade-off between precision and economy in gene expression. *Nat. Commun.* **10**, 68 (2019).
64. Petkova, M. D., Tkačik, G., Bialek, W., Wieschaus, E. F. & Gregor, T. Optimal decoding of cellular identities in a genetic network. *Cell* **176**, 844–855.e15 (2019).
65. Balakrishnan, R. et al. Principles of gene regulation quantitatively connect DNA to RNA and proteins in bacteria. *Science* **378**, eabk2066 (2022).
66. Little, S. C., Tikhonov, M. & Gregor, T. Precise developmental gene expression arises from globally stochastic transcriptional activity. *Cell* **154**, 789–800 (2013).
67. Becker, K. et al. Reverse-engineering post-transcriptional regulation of gap genes in *Drosophila melanogaster*. *PLoS Comput. Biol.* **9**, e1003281 (2013).

Publisher's note Springer Nature remains neutral with regard to jurisdictional claims in published maps and institutional affiliations.

Springer Nature or its licensor (e.g. a society or other partner) holds exclusive rights to this article under a publishing agreement with the author(s) or other rightsholder(s); author self-archiving of the accepted manuscript version of this article is solely governed by the terms of such publishing agreement and applicable law.

© The Author(s), under exclusive licence to Springer Nature America, Inc. 2025

Methods

Fly strains and genetic engineering

Drosophila melanogaster fly lines were engineered using a two-step CRISPR–Cas9-mediated transgenesis strategy to label endogenous gap genes (*hb*, *kni*, *Kr*, *gt*) with MS2 and PP7 stem-loops for live transcriptional imaging (starting from lines BDSC#78781, BDSC#78782). First, CRISPR–Cas9 was used to excise coding and regulatory regions, replacing them with a 2attp-dsRed cassette. Proper deletions were confirmed by PCR and immunostaining, and the resultant lines were referred to as gene-null backgrounds. In the second step, wild-type sequences with appropriate MS2 or PP7 insertions were cloned into 2attB vectors and integrated at the null locus using PhiC31-mediated recombination. This generated lines expressing intronic or 3′-UTR-tagged transcripts (Extended Data Fig. 1a). Additional dual-color constructs (for example, interlaced MS2–PP7 and intron + 3′-UTR MS2–PP7) were created to assess imaging error and elongation dynamics (Extended Data Fig. 2). A variant line lacking the distal *hb* enhancer was generated by replacing it with a lacZ fragment. Similarly, a line lacking the *kni* distal enhancer was generated. See Supplementary Information Section 3 for further details.

Live imaging and embryo preparation

Embryos (both sexes) were collected 2–2.5 h post egg-laying and mounted dorsal-side up on a heptane-glue-coated gas-permeable membrane, immersed in Halocarbon 27 oil and imaged under a cover glass. A custom-built two-photon laser scanning microscope was used for live imaging from NC12 to NC14. Imaging was performed with a ×40 1.3 NA objective using 920 nm and 1045 nm lasers. Each *z*-stack contained 12 slices at 1 µm intervals and was acquired every 10 s. The pixel size was 220 nm, and the image resolution was 960 × 540 pixels. See Supplementary Information Section 4 for further details.

Image processing and signal quantification

Nuclei were tracked using His2Av–mRFP-labeled histones. First, nuclei in each *z*-stack were segmented using adaptive 3D difference-of-Gaussian filtering and watersheding. Temporal tracking was then performed using a maximum-overlap Voronoi tessellation across consecutive time points. Candidate transcription spots were identified within individual nuclei using 3D median and difference-of-Gaussian filtering optimized for low signal-to-noise ratios. True spot identification and tracking were based on a Viterbi algorithm that maximized the spatiotemporal consistency of spot trajectories. Signal quantification was performed by integrating the pixel intensity within a fixed ellipsoidal volume centered on the tracked transcriptional spot, with dimensions matched to the microscope's point spread function. Local background was estimated from a surrounding shell and subtracted from the integrated signal to isolate spot-specific fluorescence. No correction for photobleaching was applied, as background fluorescence remained stable over the full duration of two-photon imaging (~80 min; Extended Data Fig. 1d). See Supplementary Information Section 5 for further details.

Spatiotemporal embryo alignment and data calibration

To minimize inter-embryo variability, all datasets were normalized in time and space. Temporal alignment was based on the duration of NC13, a robust proxy for developmental speed. Spatial alignment corrected for imaging tilt and embryo compression by least-squares minimization of expression surfaces. After alignment, residual inter-embryo variability accounted for less than 10% of the total variance on average (Extended Data Fig. 1g), enabling reliable pooling of nuclei across multiple embryos. Throughout the study, expression profiles were reconstructed by aggregating nuclei into common spatial bins along the anterior–posterior axis, with bin sizes of 2.5% and 1.5% egg length in NC13 and NC14, respectively. A global calibration to absolute units (cytoplasmic units) was performed by matching live-imaging profiles with fixed smFISH measurements (Fig. 1c). Calibration accounted for gene length, probe position and allele number, allowing accurate estimation of nascent transcript counts (Extended Data Fig. 1b,c). See Supplementary Information Sections 6.1–6.3 for further details.

Measurement error quantification

Two independent strategies were used to estimate imaging noise (Extended Data Fig. 1e). First, a *Kr* gene with interlaced MS2 and PP7 tags was imaged in dual-color mode. The resulting fluorescence intensities were compared across channels to model the heteroscedastic measurement error as a function of signal magnitude. Second, a time series autocorrelation analysis was applied, leveraging the persistence of elongating transcripts to distinguish biological from imaging noise-related fluctuations. Both approaches yielded consistent error models with additive and Poisson-like noise components (Extended Data Fig. 1f). See Supplementary Information Section 6.4 for further details.

Bayesian deconvolution of transcriptional initiation events

To infer transcription initiation events from live-imaging data, we developed a Bayesian deconvolution framework. The observed fluorescence time series, $A(t)$, was modeled as the sum of the true signal, $G(t)$, and a noise model, $\sigma(G)$, accounting for measurement uncertainty (see above). The $G(t)$ signal is described as the convolution of discrete Pol II initiation events $I(t)$ with a gene-specific kernel $\kappa(t)$, which defines the signal contribution of the MS2 cassette for each nascent transcript based on transcript length, or equivalently, on initiation timing assuming constant Pol II elongation rate K_{elo} that we measured (Extended Data Fig. 2; see below). Time was discretized to a 1 s resolution based on physical constraints of Pol II loading and elongation. The posterior distribution $P(I|A)$ over all possible initiation configurations was estimated using a custom adaptive Markov chain Monte Carlo (MCMC) sampler with block updates.

From each sampled initiation sequence $I(t)$, we computed the instantaneous transcription rate $r(t)$, defined as the number of initiation events occurring within the interval $[t - \Delta t, t]$ divided by Δt, where $\Delta = 10$ s corresponds to our measurement sampling time. This rate captures the single-allele transcriptional activity as a function of time and forms the input to subsequent steps for burst calling and time-resolved parameter estimation. See Supplementary Information Section 7.1 for further details.

Elongation rate estimation and validation

Elongation rates were estimated from dual-color experiments using constructs containing both MS2 (green) and PP7 (red) tags positioned at distinct sites within the same gene (for example, intron versus 3′ UTR). The observed delay between channels, once calibrated and deconvolved, enabled direct inference of elongation speed. To achieve this goal, we extended our deconvolution framework to simultaneously model the activity of both channels, A_g and A_r, based on a shared Pol II initiation configuration I and a single constant elongation rate parameter, K_{elo} (Extended Data Fig. 2a,b). We sampled the posterior distribution $P(I, K_{elo}|A_g, A_r)$ using our adaptive MCMC sampler. The inferred elongation rate was 1.8 ± 0.1 kb min^{-1}, consistent across genes and embryos (Extended Data Fig. 2d,e). Validation was performed by comparing the reconstructed and observed fluorescence in both channels, with residuals consistent with the noise model (Extended Data Fig. 2c). See Supplementary Information Section 7.1.6 for further details.

Fluctuation analysis of transcriptional activity

To assess transcriptional dynamics at single loci, we estimated the conditional distribution $P(r|R)$, where r is the deconvolved single-allele transcription rate from individual nuclei and R is the mean transcription rate across nuclei within a given spatiotemporal bin. This was done by pooling single-allele $r(t)$ values across time points and spatial bins for which the associated mean $R(t)$ fell within a specific range (Extended Data Fig. 3). The resulting distributions exhibited pronounced

overdispersion relative to a Poisson process, consistent with transcription initiation governed by burst-like dynamics.

To further characterize the transcriptional dynamics, we computed the autocorrelation function of $r(t)$ for each nucleus and averaged across nuclei within the spatial bin (Fig. 1f and Extended Data Fig. 5c). The averaged autocorrelation curves were fit with a decaying exponential, from which we extracted a correlated noise amplitude Σ_{AC} and a correlation time τ_{AC} that reflects the promoter switching timescale (Fig. 1g and Extended Data Fig. 5d). Notably, this timescale was approximately constant ($\tau_{AC} = 1.37 \pm 0.31$) across genes, anterior–posterior positions and nuclear cycles, consistent with an effective two-state promoter model with stable switching correlation time throughout early development. These results support the modeling assumptions underlying the subsequent burst inference. See Supplementary Information Section 7.3 for further details.

Burst inference and parameter estimation

We quantified transcriptional bursting from the single-allele transcription rate $r(t)$, computed from posterior samples of deconvolved initiation events $I(t)$. Locus states were identified using a smoothed version of $r(t)$, obtained by convolution with a quartic kernel $\kappa(t) = \frac{1}{Z(w)} \exp[-(2t/w)^4]$ with width $w = 50$ s. The binary ON–OFF signal $n(t) \in \{0,1\}$ was then defined by thresholding the smoothed trace above $r_b = g_b/w$, where $g_b = 2$ (Fig. 2a). This corresponds to detecting bursts as periods with at least two initiations within the smoothing window. Burst calling was applied to all MCMC samples of I, enabling uncertainty in the inferred burst dynamics to propagate through downstream estimates.

We computed time-dependent transcriptional parameters by averaging across posterior samples and across single-allele time series within a given spatiotemporal bin (Fig. 2b,c and Extended Data Fig. 6k). The mean transcription rate $R(t)$ was the average of $r(t)$ across nuclei. The ON probability $P_{ON}(t)$ was the fraction of nuclei for which $n(t) = 1$. The initiation rate during bursts $K(t)$ was the mean of $r(t)$ across nuclei at times where $n(t) = 1$. The mean burst duration $T_{ON}(t)$ and inter-burst interval $T_{OFF}(t)$ were computed as weighted averages over ON and OFF periods across nuclei, with weights inversely proportional to the period length, to correct for overrepresentation of longer durations at each time point.

Validation was performed using simulated datasets generated from various promoter models (two-state, three-state, cycle) with known bursting parameters (Supplementary Figs. 1 and 2). Initiation time series were simulated and convolved with gene-specific kernels to produce synthetic fluorescence signals $G(t)$. The imaging noise $\sigma(G)$ characterized above was then added to match real data. These traces were subjected to the full inference pipeline, including deconvolution, burst calling and parameter estimation. Recovered time-dependent estimates of $R(t)$, $P_{ON}(t)$, $K(t)$, $T_{ON}(t)$ and $T_{OFF}(t)$ showed strong agreement with ground truth across a range of bursting regimes, elongation times and noise levels. This analysis confirmed that the method reliably recovers time-resolved transcriptional dynamics from noisy, single-cell imaging data under biologically realistic conditions. See Supplementary Information Section 7.4 for further details.

Single gene copy parameter

Owing to early genome replication, each transcriptional spot reflects the combined activity of two unresolved sister chromatids. To infer single gene copy (SGC) bursting parameters, we transformed the effective measurements under the assumption that the two sister chromatids behave independently or weakly correlated.

The SGC transcription rate $R^{(1)}$ was computed as half the effective rate R. Assuming uncorrelated copies, we transformed the effective bursting parameters into their SGC counterpart, obtaining the SGC ON probability $P_{ON}^{(1)} = 1 - (1 - P_{ON})^{1/2}$, SGC initiation rate $K_{ON}^{(1)} = \frac{K}{2}(1 + (1 - P_{ON})^{\frac{1}{2}})$ and SGC switching correlation time $T_C^{(1)} = 2T_C/(1 + (1 - P_{ON})^{1/2})$. The SGC mean ON and OFF durations were then estimated as $T_{ON}^{(1)} = T_C^{(1)}/(1 - P_{ON}^{(1)})$ and $T_{OFF}^{(1)} = T_C^{(1)}/P_{ON}^{(1)}$, respectively.

This framework was generalized to account for inter-chromatid correlation through a coupling parameter $\eta \in [0,1]$, with $\eta = 0$ corresponding to full independence and $\eta = 1$ corresponding to perfect synchrony (Supplementary Fig. 3). Comparison with empirical transcription rate fluctuations indicated a weak correlation (Pearson's $\rho \approx 0.16$) between sister chromatids, justifying the use of single-copy parameters derived under near-independence assumptions. See Supplementary Information Sections 7.4.3 and 7.4.6 for further details.

Exploring the generality of bursting rules

To evaluate the generality of transcriptional bursting relationships, we compiled parameter estimates from four independent datasets. For *Drosophila*, we extracted bursting parameters from two live-imaging studies: one on dorsoventral genes (*ush*-wt and st2-*dpp*)[16] and one on synthetic core promoter constructs[21]. Parameters were either directly obtained or derived from reported ON probabilities and frequencies, assuming a two-state model, and are shown in Figs. 6g and 7.

We extracted the mean ON and OFF times for *GAL10* under 42 conditions from a live-imaging study[19], and computed the ON probability assuming steady state. To estimate absolute initiation rates, we calibrated the unscaled burst intensity using a 1 min residence time derived from gene length and elongation rate, conservatively adjusted for potential transcript retention. Absolute units were obtained from smFISH measurements in the −RSC (DMSO) condition, yielding an average of 13.2 ± 0.2 nascent transcripts per active site. Given the short residence time relative to T_{ON}, we assumed nascent mRNAs accumulate only during the ON state, yielding a lower-bound estimate of the initiation rate. The resulting parameter estimates are shown in Fig. 7.

For human cells, we reanalyzed single-cell time traces of 11 endogenous genes from live-imaging experiments using 24xMS2 cassettes. Original data came from two studies that imaged either 3′ UTRs (TFF1)[51] or introns (ten other genes)[9], with $\Delta t = 100$ s and trace durations averaging 11.5 h. We implemented a custom background correction by estimating each cell's background mode and dispersion from intensity histograms, then applied our deconvolution pipeline to reconstruct initiation events. Bursts were called using a smoothing window $w = 300$ s and threshold $g_b = 1$ (see above), consistent with the system's temporal resolution and claimed single-molecule sensitivity. Absolute initiation rates were inferred from estimated signal per mRNA, assuming a gene-specific dwell time of ~10 min. Final parameters were averaged over time, given the observed steady-state behavior, and are shown in Fig. 7.

Lastly, we analyzed allelic scRNA-seq data from mouse fibroblasts and embryonic stem cells. Bursting parameters for each gene were estimated from unique molecular identifier count distributions using a beta-Poisson model fit by maximum likelihood. We imposed a log-normal prior on the switching correlation time T_C (centered at 1 min) to regularize inference and mitigate identifiability issues owing to long mRNA lifetimes (median T_M, 5.3 h). Physical time units were obtained using gene-specific mRNA decay rates. Genes were retained only if they passed thresholds on parameter confidence and effective burst size, as in the original study. We then extended the framework to correct for the low capture rate and extrinsic variability. The resulting parameters were integrated in the comparative analysis of bursting rules across systems (Fig. 7b and Supplementary Fig. 5). See Supplementary Information Section 7.5 for further details.

Statistical analysis and reproducibility

All modeling and statistical analyses were performed in MATLAB 2023b using custom scripts. Parameter inference pipelines were validated against simulated datasets with known ground truth (see above), and confidence intervals were estimated by bootstrapping. For each of the ten experimental conditions, 10–20 embryos were imaged across

$N_t = 471$ time points (covering NC13 and NC14) and $N_x = 9–18$ anterior–posterior positions, yielding approximately 200 nuclei per spatial bin. Temporal and spatial binning ensured sufficient sampling for accurate estimation of higher-order statistical moments, as verified through bootstrap-derived confidence intervals.

No statistical method was used to predetermine sample size. Two embryos were excluded from the analysis in NC14: *hb* embryo no. 9 and *gt* female posterior embryo no. 7, both of which exhibited spatiotemporal misalignment consistent with developmental defects. Single-allele deconvolution was restricted to spatial bins containing at least 100 nuclei and to the time intervals [2.5,15] min in NC13 and [2.5,50] min in NC14, resulting in $N_t = 362$ effective time points. These windows were selected based on biological constraints: transcription initiates only after ~2.5 min, shuts down before mitosis in NC13 (~15 min) and becomes slightly distorted in NC14 after 50 min because of morphological changes preceding gastrulation (around 60 min). Experiments were not randomized, as embryos were assigned to conditions based on known genotypes from controlled breeding. The investigators were not blinded to group allocation during the experiments or outcome assessment, as measurements were standardized, identical across conditions and not influenced by group assignment.

Reporting summary

Further information on research design is available in the Nature Portfolio Reporting Summary linked to this article.

Data availability

Original movies are available upon request. Full processed datasets are provided as source data and are available on Zenodo (https://doi.org/10.5281/zenodo.15396340)[68].

Code availability

Full code is available on GitLab (https://gitlab.pasteur.fr/tglab/liveburstrulepaper).

References

68. Zoller, B. et al. Gene activity predicts transcriptional bursting dynamics through coupled on and off periods. *Zenodo* https://doi.org/10.5281/zenodo.15396340 (2025).

Acknowledgements

We thank members of the Gregor laboratory for their discussions and comments on the manuscript. We also thank E. Bertrand, M. Lagha, T. Lenstra, M. Levine, O. Radulescu, T. Sokolowski, G. Tkačik, E. Wieschaus and J. Yuly for comments and discussion at various stages. We thank D. Larson and T. Lenstra for sharing data. This work was supported in part by the US National Science Foundation, through the Center for the Physics of Biological Function (PHY-1734030 to T.G.), and by National Institutes of Health Grants R01GM097275, U01DA047730 and U01DK127429 (to T.G.). M.L. received a Human Frontier Science Program fellowship (LT000852/2016-L), EMBO long-term postdoctoral fellowship (ALTF 1401-2015) and Rothschild postdoctoral fellowship.

Author contributions

M.L., B.Z. and T.G. conceptualized the project. P.C. designed and constructed the microscope and performed data acquisition of all live-imaging experiments. M.L. engineered genetic constructs and produced fly lines. B.Z. processed raw data and performed image and data analysis. M.L., B.Z. and T.G. wrote the original manuscript and reviewed, edited and proofed the final text. M.L. and T.G. secured the funding.

Competing interests

The authors declare no competing interests.

Additional information

Extended data is available for this paper at https://doi.org/10.1038/s41594-025-01615-4.

Supplementary information The online version contains supplementary material available at https://doi.org/10.1038/s41594-025-01615-4.

Correspondence and requests for materials should be addressed to Thomas Gregor.

Peer review information *Nature Structural & Molecular Biology* thanks the anonymous reviewers for their contribution to the peer review of this work. Primary Handling Editor: Dimitris Typas, in collaboration with the *Nature Structural and Molecular Biology* team. Peer reviewer reports are available.

Reprints and permissions information is available at www.nature.com/reprints.

https://doi.org/10.1038/s41594-025-01615-4

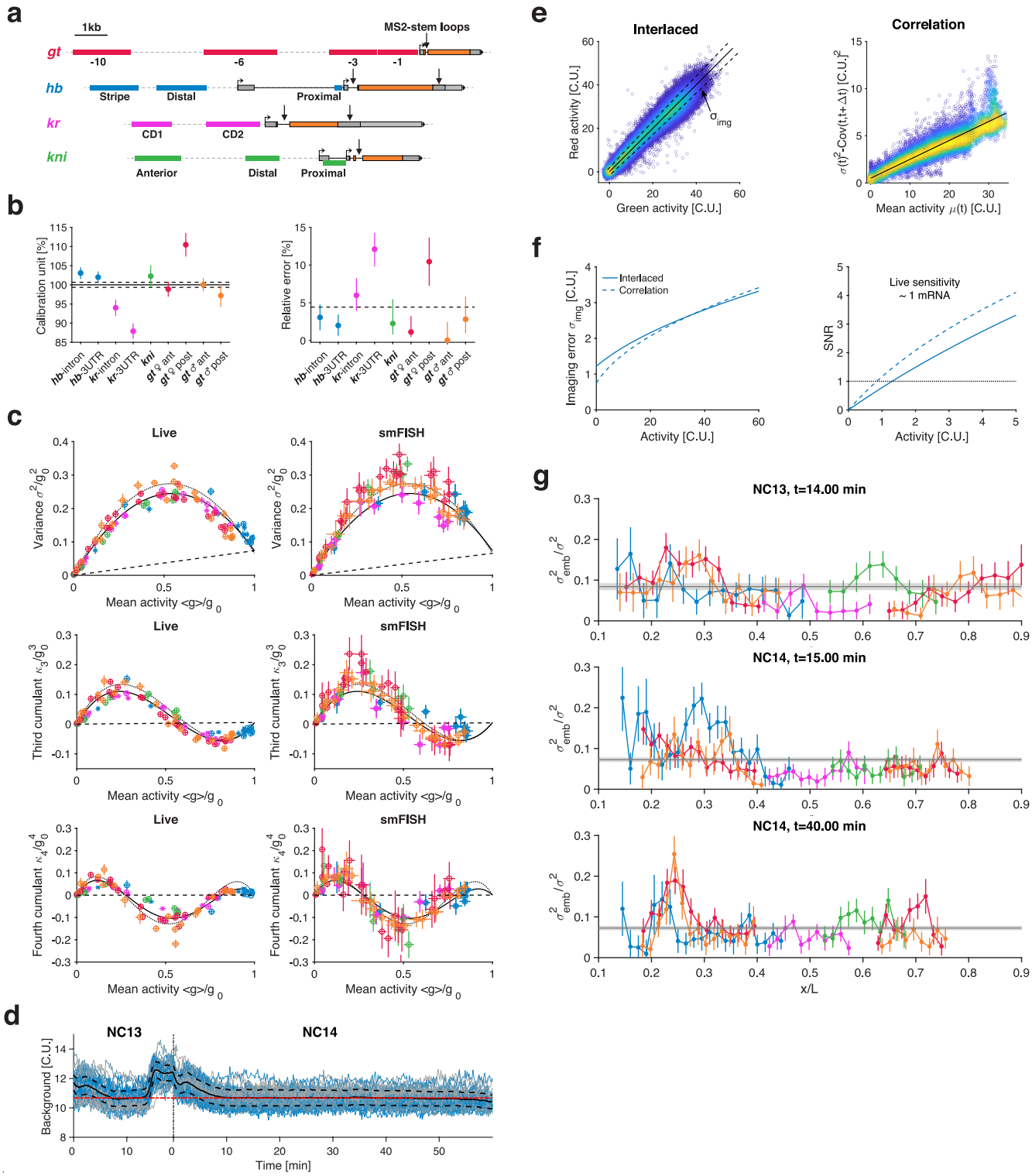

Extended Data Fig. 1 | See next page for caption.

https://doi.org/10.1038/s41594-025-01615-4

Extended Data Fig. 1 | Signal calibration, measurement error and embryo-to-embryo variability. (a) The four trunk gap genes – *giant* (*gt*), *hunchback* (*hb*), *Kruppel* (*Kr*), and *knirps* (*kni*) – were imaged using MS2/PP7 stem-loop labeling. Stem-loop cassettes (black arrow) were inserted in either intronic or 3'UTR regions. These genes feature distinct *cis*-regulatory architectures, differing in numbers of promoters, enhancers (colored boxes), and regulatory sequence composition (for example, TF binding motifs, core promoter elements). **(b)** Relative calibration unit (left) and relative error (right) for each gap gene construct related to Fig. 1c. Calibration of live transcriptional signals to absolute units was achieved by matching spatial activity profiles (averaged over nuclei in 2.5% AP bins during a 5-min window in NC13) with smFISH-based measurements (Zoller et al., 2018). (Left) A global calibration unit was obtained from a joint fit across all genes (horizontal black line, ±1 s.e. as dashed lines). Individual fits per construct (colored circles) are shown as a percentage of the global value. (Right) Relative calibration errors remain below 5%, with error bars representing 68% confidence intervals. **(c)** Higher-order cumulants (mean, variance, 3rd and 4th) of transcriptional activity from live imaging closely match those from smFISH (Zoller et al., 2018). Live data were binned spatially (2.5% AP) and temporally (5 min window in NC13), converted from cytoplasmic mRNA units (C.U.) to Pol II counts for a 3.3 kb gene. Cumulants were normalized using g_0, the intercept of a Poisson background (dashed line) and a polynomial fit (solid for live, dotted for smFISH). g_0 represents the mean number of Pol II on a 3.3 kb gap gene at peak activity; it is estimated at 13.6 (live) and 15.2 (smFISH), a 12% difference. The higher cumulants versus mean relationships from live imaging and smFISH closely match (black solid versus dotted line), confirming the quantitative accuracy and proper calibration of our live assay. These independent methods, one involving fixation (smFISH), the other gene editing (MS2/PP7), validate each other and indicate that our synthetic modifications do not measurably affect endogenous transcriptional output. **(d)** Background intensity is temporally stable, showing no bleaching under two-photon imaging. Background levels (C.U.) were measured in nuclei from weakly expressing regions ($x/L \in [0.48, 0.60]$) across 10 *hb*-MS2 embryos. The mean background (black line, ±1 s.d., $\sigma_b = 0.53$) is stable, with only transient deviations during mitosis due to nuclear envelope dynamics (breaking and reformation) affecting MCP-GFP concentration. Outside mitosis, it closely matches the overall median (red dashed line), confirming the absence of bleaching under two-photon imaging. **(e)** Imaging noise was assessed via two independent methods. (Left) An interlaced MS2/PP7 cassette in *Kr* (first intron) labeled by MCP-GFP and PCP-mCherry was used to compare red/green channel intensities. Deviations orthogonal to the diagonal (slope one) quantify the imaging spread σ_{img}, modeled as $\sigma_b^2 + \alpha I$, where σ_b^2 is background noise and αI represents Poisson shot noise based on mean intensity I. Dashed lines show the resulting fit for σ_{img}^2, corresponding to ±1 s.d. around the diagonal. (Right) In a second approach, transcriptional time series were analyzed to separate uncorrelated imaging noise from biological fluctuations that are correlated due to the elongation of tagged nascent transcripts. Mean $\mu(t)$, variance $\sigma^2(t)$, and lagged covariance $Cov(t, t+\Delta t)$ were computed across nuclei (1.5–2.5 AP bins) and for all measured genes. Imaging variance σ_{img}^2 estimated as $\sigma^2(t)$-Cov$(t, t+\Delta t)$ is plotted as a function of $\mu(t)$ for all time points. We estimated average σ_{img}^2 by fitting the data with $\sigma_b^2 + \alpha\mu$ (solid line). Overall, the fractional imaging variability σ_{img}^2/σ^2 is ~5%. **(f)** Both methods in (**e**) produce consistent estimates of imaging noise. The signal-to-noise ratio (SNR = μ/σ_{img}) approaches unity for low expression ($\mu \approx 1$), indicating near single-molecule sensitivity. **(g)** Fractional embryo-to-embryo variability σ_{emb}^2/σ^2, calculated as the ratio of inter-embryo variance (that is, variance of the mean activity across embryos) to total variance, is ~10%, across all gap genes and time points. Since total variance $\sigma^2 = \sigma_{emb}^2 + \sigma_{img}^2 + \sigma_{nuc}^2$, and imaging ($\sigma_{img}^2$) and embryo variability (σ_{emb}^2) are minor components, the majority of transcriptional variability arises from nucleus-to-nucleus fluctuations (σ_{nuc}^2). Together, (**e**–**g**) support using total variance σ^2 as a robust proxy for biologically relevant noise from transcriptional bursting.

https://doi.org/10.1038/s41594-025-01615-4

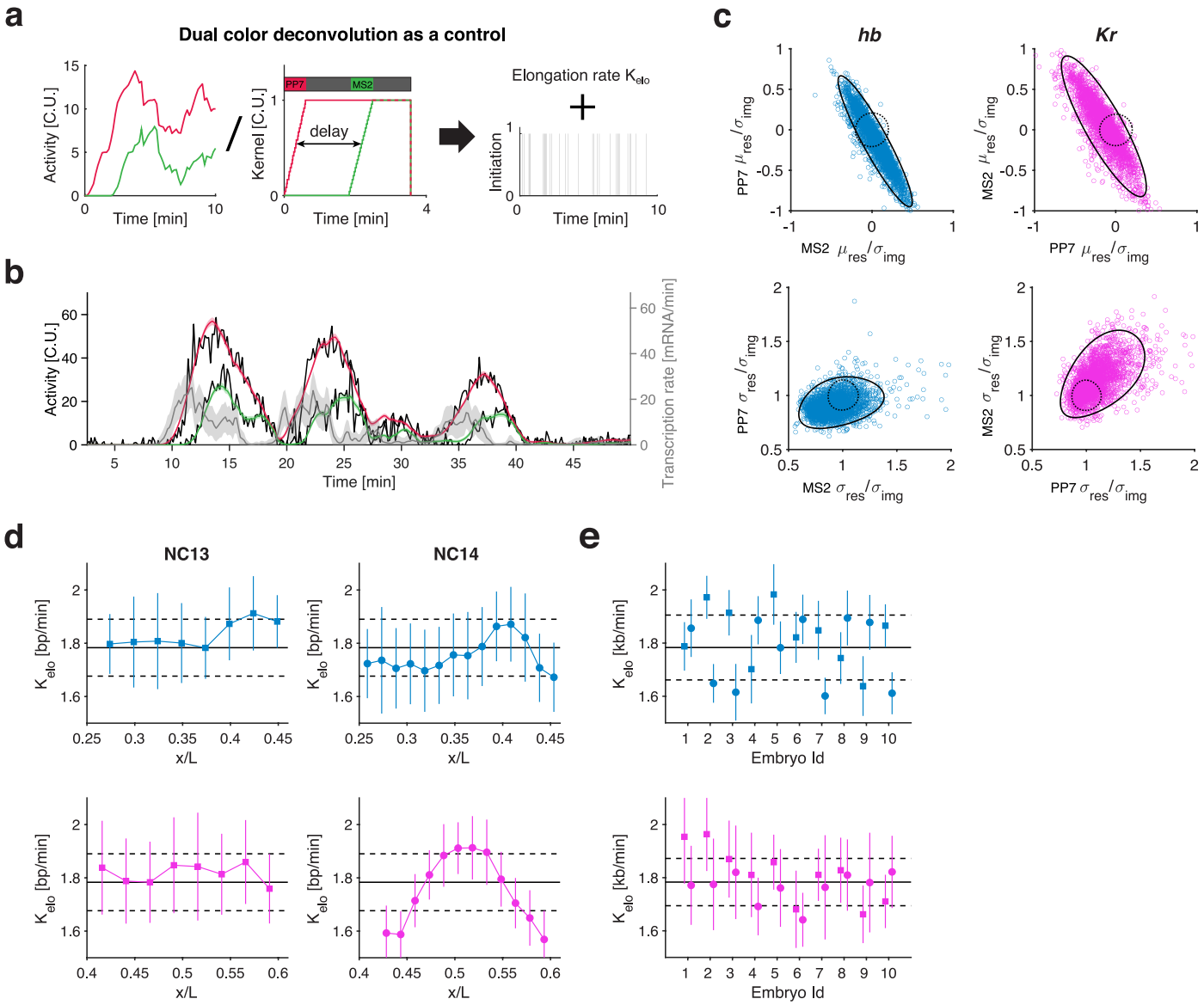

Extended Data Fig. 2 | Dual color measurements to validate single-cell deconvolution and measure elongation rate. **(a)** Validation of the kernel assumptions underlying the deconvolution of initiation events from single-allele transcription time series, using dual-color confocal imaging of *hb* and *Kr*. For *hb* (*Kr*), fly lines were generated with MS2 (PP7) stem-loop cassettes in the first intron and PP7 (MS2) cassettes in the 3′UTR. Both lines were visualized using MCP-GFP (green) and PCP-mCherry (red). As the two fluorescent signals are correlated via the elongation process, the paired time series impose stricter constraints on the underlying initiation events, making them an effective test of the deconvolution method. Deconvolution is performed jointly on each channel (that is, a single train of polymerases must explain both signals) using two kernels tailored to the stem-loop positions and satisfying the key assumptions: (i) constant, deterministic elongation rate; (ii) no Pol II pausing or dropping in the gene body; (iii) absence of co-transcriptional splicing; and (iv) fast termination. Additionally, the dual-color configuration allows estimation of the average elongation rate based on the time delay between the two signals and the known genomic distance between insertion sites. **(b)** Dual-color signal reconstruction from deconvolved single-allele time series (black lines: raw data). The transcription rate (gray line with ±1 s.d. envelope) is inferred from a single allele's measured green and red traces. The denoised reconstructed signals (green and red, with ±1 s.d.) are obtained by re-convolving the inferred transcription rate with the appropriate kernel per channel. The close agreement between reconstructed and raw signals supports the validity of the kernel assumptions (see **c**). **(c)** Distribution of residuals between measured and reconstructed dual-color signals. Normalized residuals were computed as the difference between raw and reconstructed signals (panel **b**), divided by the standard deviation of imaging noise. This was done per allele for *hb* ($N = 2666$, blue) and *Kr* ($N = 2594$, pink). The spread of mean and standard deviation values of these residuals (black ellipse, 95% confidence) closely matches the expected distribution for a perfect model (dotted ellipse, 95% confidence), indicating good reconstruction fidelity. **(d–e)** Estimated elongation rate K_{elo} from dual-color measurements. **(d)** Mean elongation rate as a function of AP position, averaged over nuclei from 10 embryos, for both *hb* (blue) and *Kr* (pink) in NC13 (squares) and NC14 (circles). Error bars indicate the standard deviation across embryo means. **(e)** Per-embryo elongation rates (symbols and color scheme as in **d**), with error bars showing standard deviation across AP positions. Elongation rate is consistent across genes and nuclear cycles, with a global estimate of $K_{elo} = 1.8 \pm 0.1$ kb/min (black line ±1 s.d., dashed).

https://doi.org/10.1038/s41594-025-01615-4

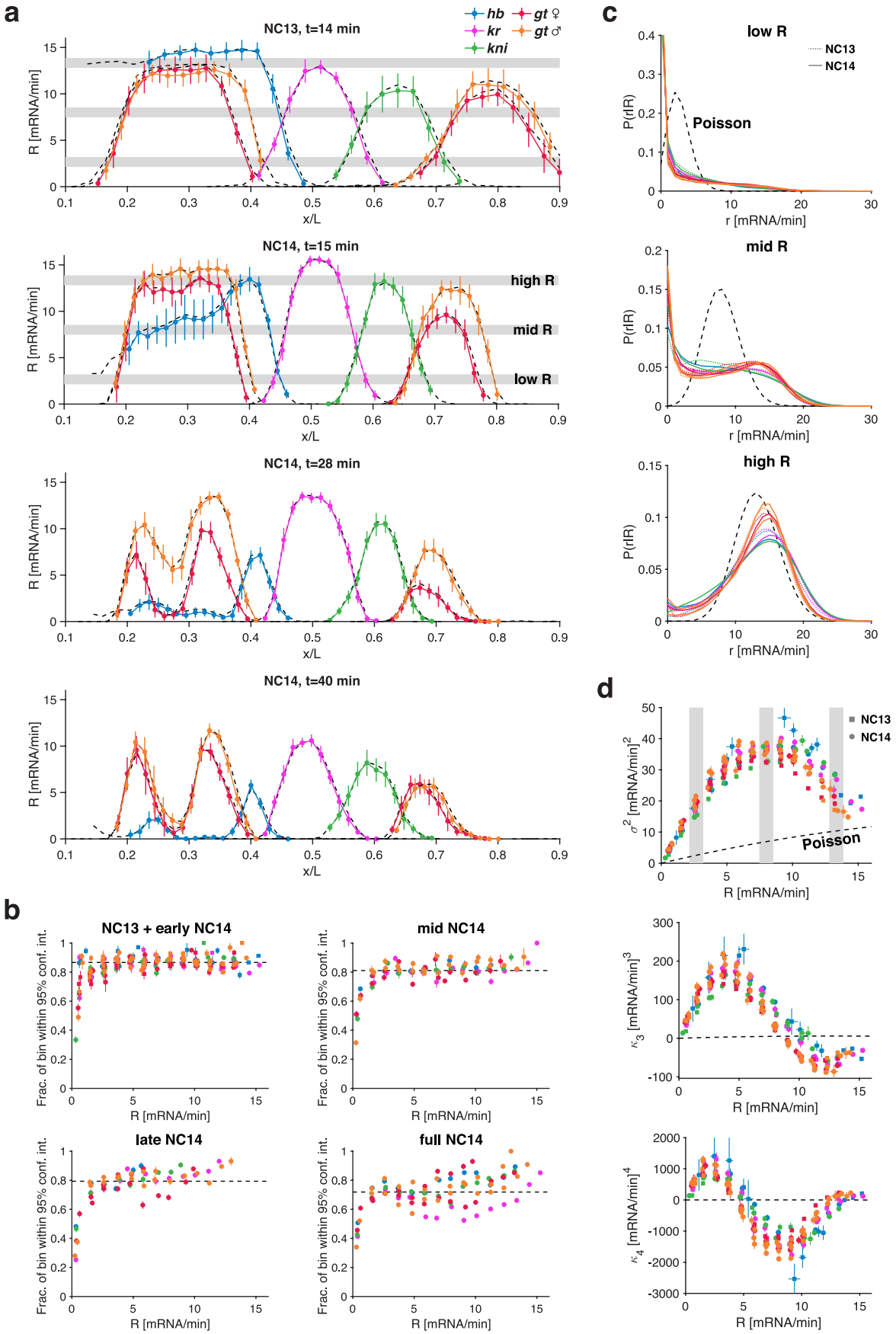

Extended Data Fig. 3 | See next page for caption.

https://doi.org/10.1038/s41594-025-01615-4

Extended Data Fig. 3 | Single-allele transcription rate distributions reveal common bursting characteristics. (a) Snapshots of the mean transcription rate R for each gap gene as a function of AP position during late NC13 and early, mid, and late NC14 (specified by time t after mitosis). Colored profiles represent the average deconvolved single-allele transcription rate per AP bin (width: 2.5% in NC13, 1.5% in NC14), averaged over all nuclei and time points (10 s resolution). Black dashed lines show the mean activity (as in Fig. 1c), normalized by the effective elongation time (see Extended Data Fig. 4a, Methods). The strong agreement between measured and deconvolved profiles supports the validity of our approach. Error bars represent ±1 s.d. across embryo means. In total, we analyzed $N_g = 7$ effective genes (accounting for *gt* sex-specificity and spatial regions), over $N_t = 362$ time points and $N_x = 9–18$ AP positions, yielding 33′214 spatiotemporal bins, each averaging ~200 nuclei (single allele per nucleus). Remarkably, all gap genes reach a similar peak average transcription rate: $R_{max} = 14.8 \pm 0.9$ mRNA/min. **(b)** Fraction of spatiotemporal bins (indexed by position x and time t) whose transcription rate distribution $P(r|x,t)$ is consistent with the conditional distribution $P(r|R)$, computed by pooling nuclei from multiple bins with similar mean rate R (see panel **c**). We calculated 95% confidence intervals for the cumulative distribution of $P(r|R)$, and assessed for each bin whether its individual cumulative distribution lay within this envelope. This analysis was repeated across four developmental windows: NC13 ($6.5 \le t$ min after mitosis), early NC14 ($7.5 \le t < 20.5$ min), mid NC14 ($20.5 \le t < 34.5$ min), and late NC14 ($34.5 \le t < 48$ min), as well as across the full NC14 period ($7.5 \le t < 48$ min). Within each time window, bins with the same R exhibit highly similar distributions (median agreement >80%, dashed line), justifying the pooling. However, pooling across the full NC14 window introduces temporal variability, suggesting that $P(r|R)$ may evolve with time. **(c)** Conditional distributions $P(r|R)$ of single-allele transcription rates at low ([2.1,3.2]), mid [7.5,8.5]), and high [12.8,13.9]) mean transcription rate R (gray bands in **a**, **d**), computed over 1-min intervals in NC13 (dotted lines) and early NC14 (solid lines). Despite gene identity, distributions at a given R collapse, suggesting a shared transcriptional regime. All distributions deviate from the Poisson expectation (dashed black line), especially at low and mid R, where they exhibit bimodality: a peak near zero (non- or weakly-transcribing alleles) and an overrepresentation of high-expression alleles. These features are characteristic of transcriptional bursting. **(d)** Second (variance), third, and fourth cumulants of single-allele transcription rates plotted against the mean rate R, for NC13 (squares) and early NC14 ($7.5 \le t < 20.5$ min; circles). Cumulants are estimated in 1-min intervals. All deviate from the Poisson expectation ($\sigma^2 = \kappa_3 = \kappa_4 = R$; dashed line), except at the lowest and highest R. The mean–variance relationship forms a concave parabola, consistent with a two-state bursting model where modulation of P_{ON} underlies changes in R[23]. This supports a universal bursting mechanism where gap genes transition from fully OFF ($P_{ON} = 0$) to fully ON ($P_{ON} = 1$). Vertical gray bands mark low, mid, and high R as in panel (**a**).

https://doi.org/10.1038/s41594-025-01615-4

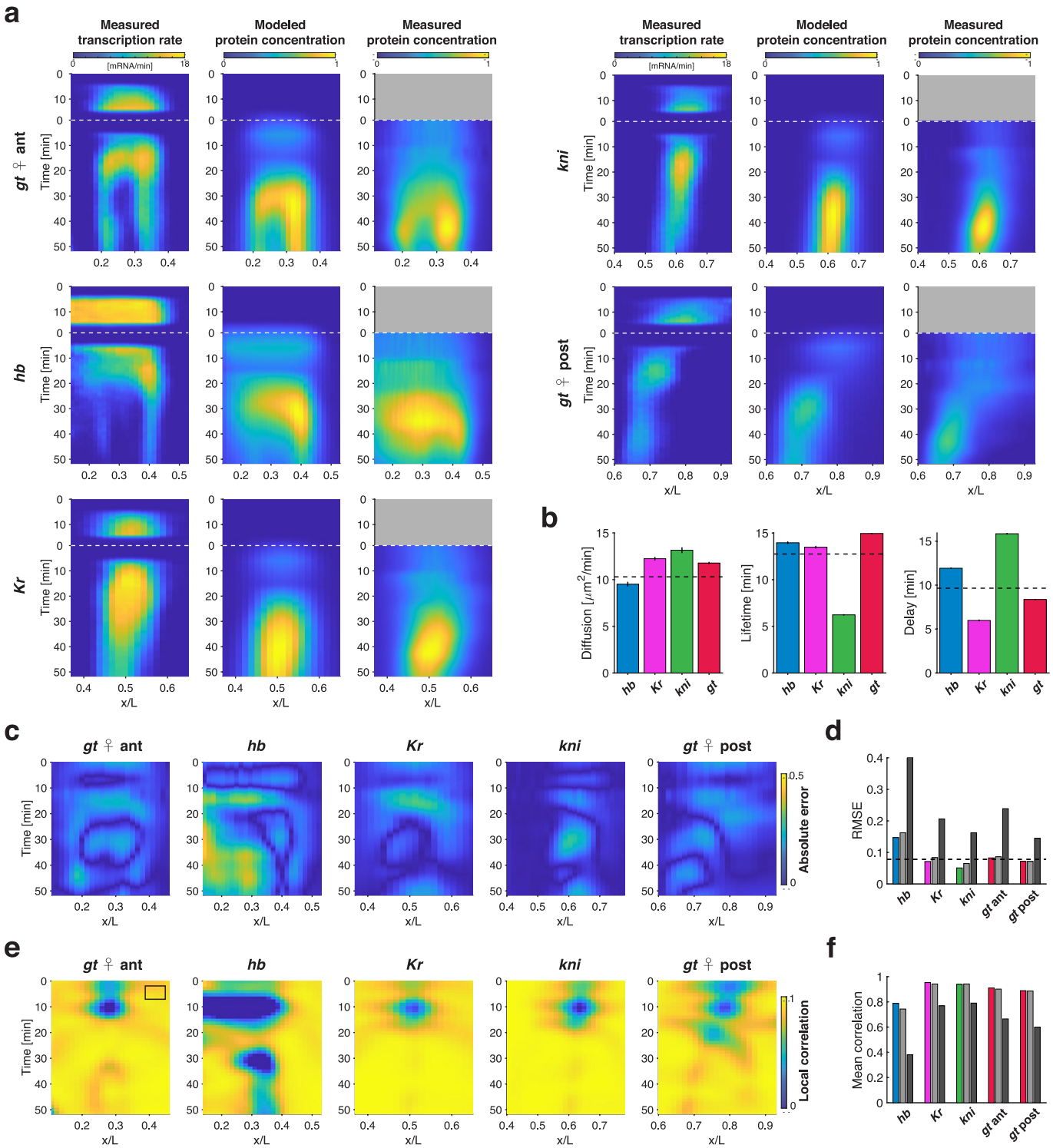

Extended Data Fig. 4 | See next page for caption.

https://doi.org/10.1038/s41594-025-01615-4

Extended Data Fig. 4 | Mean transcription rate explains dynamic pattern establishment. (a) A simple model to estimate protein accumulation from measured mean transcription rates. The mean transcription rate (left column), across space and time, is computed by normalizing the measured activity by the elongation time and applying a minor correction for the loop-insertion delay (<1 min). Horizontal white dashed lines mark the mitotic transition from NC13 to NC14. Protein accumulation (middle column) is modeled as the convolution of the transcription rate with a kernel that captures protein decay, diffusion, and a combined time delay due to mRNA export, translation, and nuclear import. This model involves three free parameters: protein lifetime, diffusion constant, and time delay (see panel **b**), which were optimized to minimize the mean squared error relative to gap gene protein patterns measured via antibody staining of carefully staged embryos (right column; Dubuis et al., 2013). Minor residual differences between model and experiment can be attributed to staging inaccuracies or, in the case of *hb*, to unmodeled maternal mRNA contributions (see **c**). **(b)** Estimated model parameters for protein accumulation, as described in (**a**). Parameters were either fitted individually for each gene (colored bars) or globally across all genes (dashed lines, used for middle column in **a**). The inferred values are broadly consistent with previous estimates[67]. **(c)** Quantitative comparison between modeled and measured protein patterns shown in (**a**). Absolute errors were computed across the patterns in space and time. The generally low errors confirm a strong match between model and experiment. For *hb*, larger discrepancies are observed in the anterior, likely due to maternal mRNA contributions not captured by the model. **(d)** Overall root mean square errors (RMSE) between the measured protein pattern (from antibody staining), the modeled protein pattern (with either individual or global parameters), and the transcription rate data. Protein models (individual: colored, global: light gray) yield low RMSE values (mean 0.09), while using the transcription rate directly leads to higher error (mean 0.23), mainly due to the time lag between transcription and protein accumulation. For reference, the RMSE between live and fixed (smFISH) mean profiles (see Fig. 1c) is shown as a dashed line at 0.08. **(e)** Structural comparison of modeled and measured protein patterns, assessing pattern shape and features (for example, peaks, boundaries). We computed the local spatiotemporal correlation (akin to a structural similarity index without luminance or contrast terms) using a 4-AP-bin (6% egg length) and 5-min window (black rectangle). Local correlations are generally high (near 1), indicating strong structural agreement. Discrepancies mainly occur during the first 20 minutes, when few stained embryos were available for accurate staging (see Dubuis et al., 2013). As in panel **c**, *hb* displays residual differences at later stages due to unmodeled maternal input. **(f)** Mean correlation across space and time between measured transcription rate (dark gray), modeled protein concentration (individual: color; global: light gray), and measured protein pattern. Correlation values were averaged over the full spatiotemporal pattern using the local measure from (**e**). The modeled protein patterns show high agreement with experimental data (mean correlation ≈ 0.9), while transcription rates alone correlate less well (≈0.6), consistent with expected temporal lag between transcription and protein levels.

https://doi.org/10.1038/s41594-025-01615-4

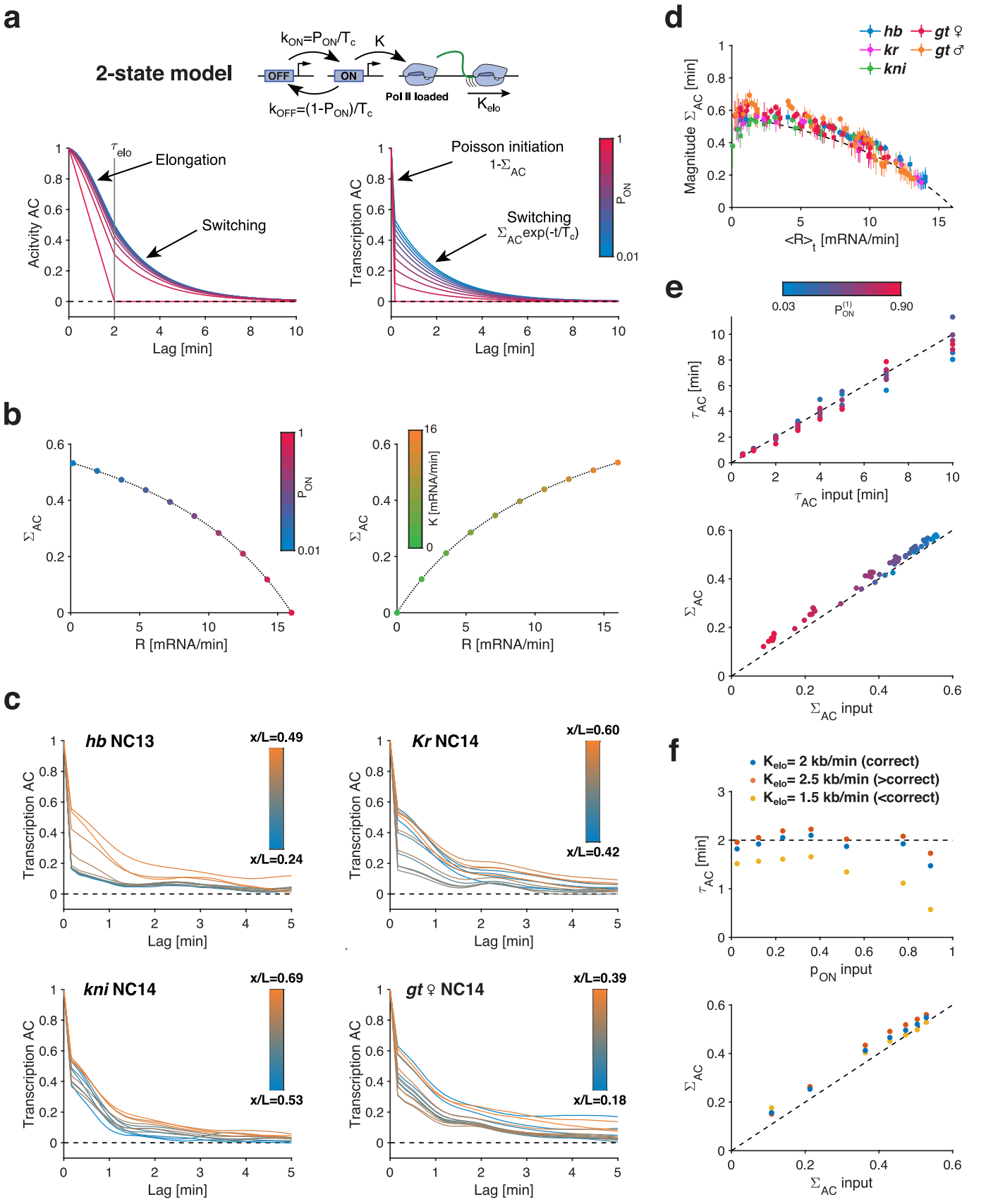

Extended Data Fig. 5 | See next page for caption.

https://doi.org/10.1038/s41594-025-01615-4

Extended Data Fig. 5 | Single-allele transcription rate fluctuations reveal key bursting characteristics. (a) Interpreting auto-correlation functions using a two-state model of transcriptional bursting. In this model (top), a single gene copy switches stochastically between OFF and ON states with rates k_{OFF} and k_{ON}, respectively. While ON, Pol II loads at a rate $K^{(1)}$ and elongates at rate K_{elo}. The superscript (1) indicates parameters for a single gene copy. The auto-correlation function (AC) was computed using: a switching correlation time $T_C^{(1)} = 1/(k_{OFF} + k_{ON}) = 2$ min, a Pol II elongation time $\tau_{elo} = L_g/K_{elo} = 2$ min (where L_g is the gene length) and an initiation rate $K^{(1)} = 8$ mRNA/min. The steady-state ON-probability $P_{ON}^{(1)} = k_{ON}/(k_{ON} + k_{OFF})$ ranges from 0 to 1 (blue to red). While promoter switching introduces temporal correlations in the transcriptional activity ('Activity AC'), these are often masked by elongation-induced correlations, especially when $T_C^{(1)} \leq \tau_{elo}$ (left). However, using deconvolved single-allele transcription rates removes elongation effects and reveals pure switching dynamics ('Transcription AC', right), allowing direct estimation of $T_C^{(1)}$ by exponential fitting of the decay. **(b)** Expected dependence of the magnitude of correlated fluctuations Σ_{AC}, on the ON-probability $P_{ON}^{(1)}$ (left) and initiation rate $K^{(1)}$ (right), for fixed $T_C^{(1)} = 2$ min. (Left) At fixed $K^{(1)}$, as $P_{ON}^{(1)}$ increases, the transcription rate $R = 2K^{(1)}P_{ON}^{(1)}$ (for 2 sister chromatids) increases, while Σ_{AC} decreases and vanishes at $P_{ON}^{(1)} = 1$, consistent with the Poisson (constitutive) regime. This trend agrees with data in panel (**d**). (Right) At fixed $P_{ON}^{(1)}$, increasing $K^{(1)}$ raises both R and Σ_{AC}, contrary to observations. In both cases, the dotted line represents the exact solution, well approximated by $\Sigma_{AC} = \Delta t K^{(1)}(1 - P_{ON}^{(1)})/(1 + \Delta t K^{(1)}(1 - P_{ON}^{(1)}))$, with $\Delta t = 10$ s (data sampling interval). **(c)** Auto-correlation functions of single-allele transcription rates measured in gap genes, averaged over time and grouped by AP position (color-coded). **(d)** Magnitude of correlated fluctuations Σ_{AC} as a function of mean transcription rate R, computed from the gap gene data. All genes collapse onto a single curve, indicating a universal trend. As R increases, Σ_{AC} decreases, consistent with a transition toward a Poisson regime. The trend is captured by a model with a constant $K^{(1)} = 8.2$ mRNA/min and variable $P_{ON}^{(1)}$ (dashed line; see Methods and panel **b**). **(e)** Deconvolution reliably recovers correlation times and fluctuation magnitudes. Using the Gillespie algorithm, we simulated transcription traces under the two-state model for various $P_{ON}^{(1)}$ (from 0.03 to 0.9) and $T_C^{(1)}$ (from 0.5 to 10 min), with 200 simulated nuclei per condition (50 min recordings). Following deconvolution, we estimated $T_C^{(1)}$ and Σ_{AC} by fitting an exponential to the transcription AC. Both parameters were recovered accurately with minimal bias. Color encodes $P_{ON}^{(1)}$; dashed line indicates slope 1. **(f)** Assessing bias from elongation rate misestimation during deconvolution. Simulations were repeated as in (**e**), with $T_C^{(1)} = 2$ min, and deconvolution performed using incorrect elongation rates: overestimated (orange), underestimated (yellow), or accurate (blue). While estimates remain broadly consistent, underestimating elongation rate introduces greater bias, especially at high $P_{ON}^{(1)}$.

https://doi.org/10.1038/s41594-025-01615-4

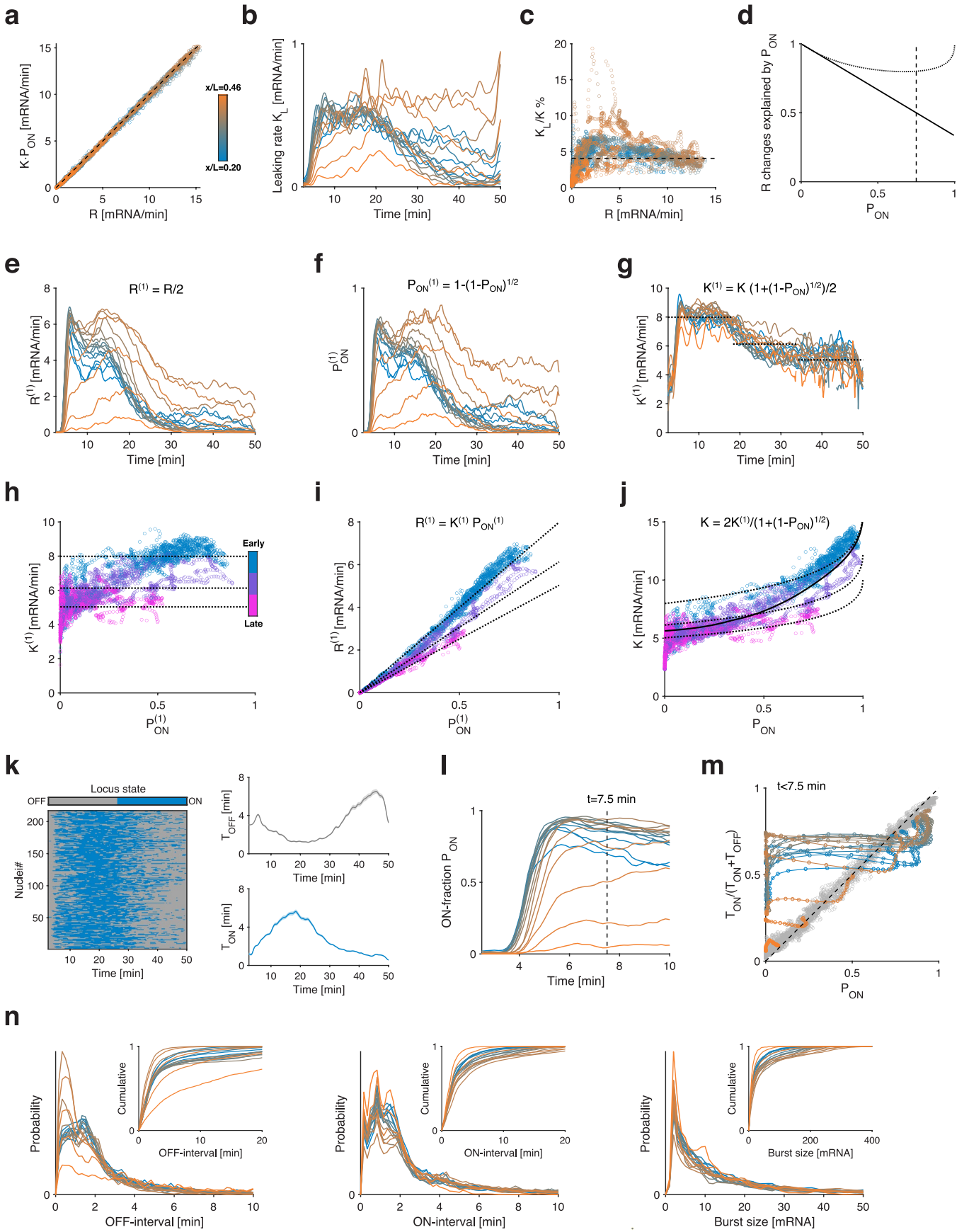

Extended Data Fig. 6 | See next page for caption.

https://doi.org/10.1038/s41594-025-01615-4

Extended Data Fig. 6 | Direct estimation of instantaneous mean transcription parameters for *hunchback* in NC14. (a) Transcription rate R versus the product of initiation rate K and ON-probability P_{ON} for *hb* in NC14 across all time points and AP positions (color-coded as in Figs. 2 and 3). As expected, $R = K \cdot P_{ON}$ by construction. **(b)** Leaking rate K_L as a function of time in NC14 for all AP positions. K_L is computed by averaging single-allele transcription rates conditioned on the locus being OFF (in contrast to K, computed conditioned on ON allele). **(c)** Leaking rate as a percentage of the initiation rate, K_L/K, plotted against transcription rate R. Across all conditions, K_L remains below 5% of K, indicating well-defined bursting and minimal transcriptional leakage. **(d)** Fraction of changes in R attributable to P_{ON}, plotted as a function of P_{ON}. The black line shows $d\log P_{ON}/dP_{ON}$ normalized by $d\log K/dP_{ON} + d\log P_{ON}/dP_{ON}$. The dotted line accounts for two independent sister chromatids (see panels **e**–**j**). Results indicate that changes in R are predominantly driven by P_{ON}. **(e–g)** Inferred single-gene-copy (SGC) parameters for *hb* in NC14, under the assumption of two independent sister chromatids (Methods). Color encodes AP position as in panel (**a**). **(e)** The SGC transcription rate $R^{(1)}$ and **(f)** the SGC ON-probability $P_{ON}^{(1)}$ closely follow their effective counterparts R and P_{ON}. **(g)** In contrast, the SGC initiation rate $K^{(1)}$ is spatially uniform but varies over time. It decreases by ~38% during NC14, from 8.0 mRNA/min (early, first dotted line) to 5.0 mRNA/min (late, third dotted line), with most of the change occurring between 16 and 34 min (second dotted line at 6.1 mRNA/min). The resulting mean Pol II spacing, $K_{elo}/K^{(1)} = 303 \pm 73$ bp, aligns with classical EM estimates (330 ± 180 bp) from Miller spreads[41]. **(h–j)** Temporal variation in $K^{(1)}$ and chromatid independence explain the observed dependence of K on P_{ON}. Colors denote three NC14 windows: early (cyan, 2.5–16.7 min), mid (purple, 16.7–34.2 min), and late (magenta, 34.2–50 min). **(h)** Most variation in $K^{(1)}$ arises from time rather than $P_{ON}^{(1)}$; dotted lines mark the values from panel (**g**). **(i)** $R^{(1)}$ scales nearly linearly with $P_{ON}^{(1)}$, with modest deviations explained by temporal changes in $K^{(1)}$. Dotted lines show slopes matching the $K^{(1)}$ values from panels (**g**) and (**h**). **(j)** Under the independent chromatid assumption, the effective rate K depends on both P_{ON} and time-varying $K^{(1)}$. As P_{ON} increases, the likelihood of simultaneous transcription from both chromatids increases, explaining a ~ 2-fold rise in K. The additional time variation in $K^{(1)}$ accounts for a total ~3.2-fold increase in K. The predicted relationship (black line) agrees well with observed data, supporting the idea that K depends weakly on P_{ON} directly. **(k)** Binarized heatmap from Fig. 2c showing instantaneous mean OFF-times (T_{OFF}, gray) and ON-times (T_{ON}, blue), computed as weighted averages across all nuclei (Methods). Weights reflect the inverse of the number of time points within each period. **(l)** Zoom into the first 10 minutes of NC14 from Fig. 2f reveals a rapid transient in P_{ON} for *hb*. A vertical dashed line at 7.5 min marks the transition from the post-mitotic transient phase to a near steady state, as also shown in panel (**c**). **(m)** Evidence for an initial out-of-steady-state regime. Beyond 7.5 min, $P_{ON} \approx T_{ON}/(T_{ON} + T_{OFF})$ holds (gray circles lie along the diagonal; see Fig. 3b). Prior to that (~3–7.5 min), strong deviations at all positions (color curves) indicate rapid post-mitotic relaxation toward steady state. **(n)** Distributions and cumulative distributions of OFF-times, ON-times, and burst sizes across AP positions (color-coded). These are compiled across all alleles and time points at a given position (see heatmaps in k and Fig. 2b). Since they reflect non-stationary dynamics (see Figs. 2d-f and 3a), these distributions are not well-suited for direct interpretation, such as assessing deviations from the exponential OFF- and ON-interval distributions expected under a stationary two-state model.

https://doi.org/10.1038/s41594-025-01615-4

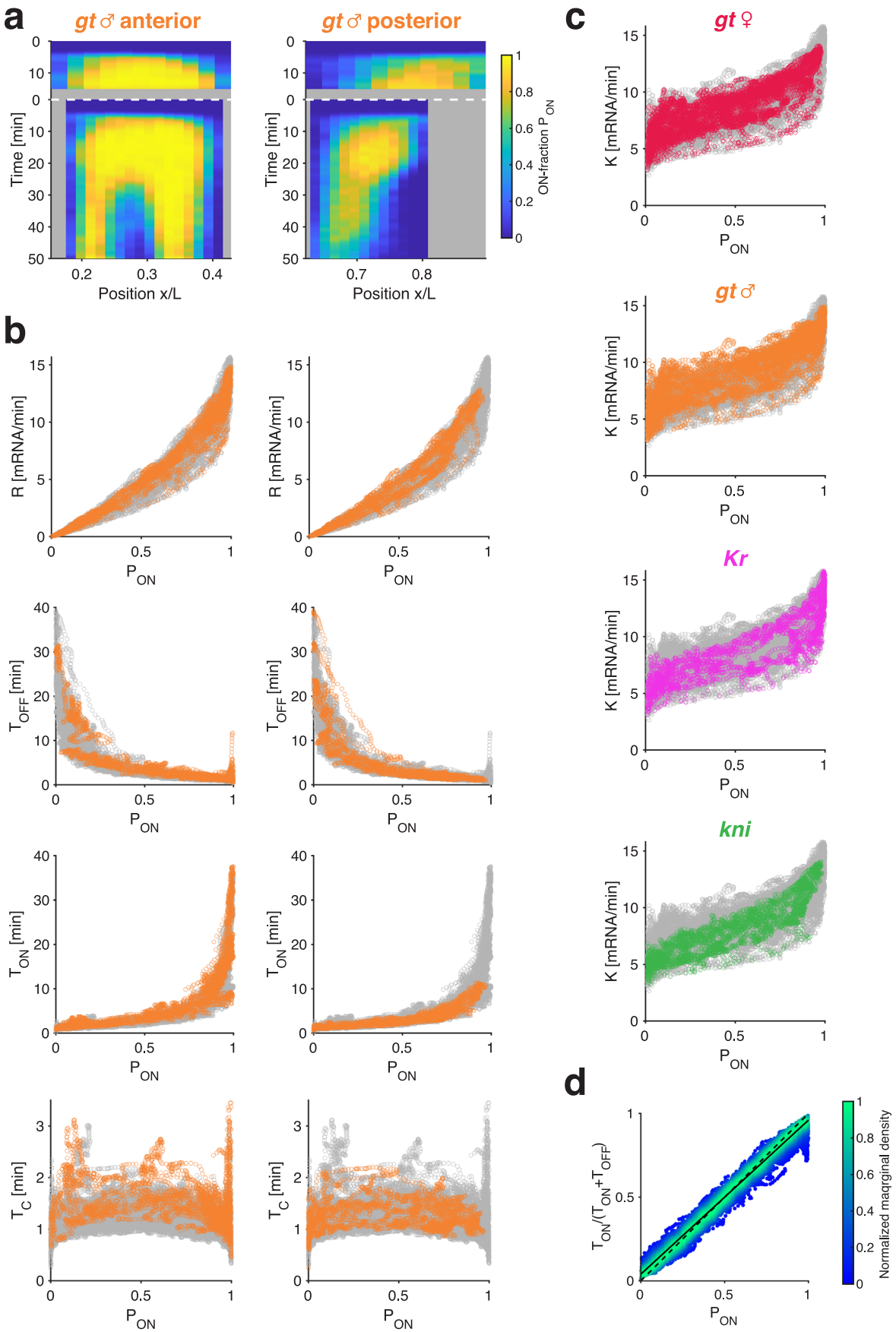

Extended Data Fig. 7 | See next page for caption.

https://doi.org/10.1038/s41594-025-01615-4

Extended Data Fig. 7 | Further transcription parameters collapse. **(a)** Kymograph of ON-probability P_{ON} for *gt* transcription in male embryos, shown as a function of AP position and time. As with other gap genes, the spatiotemporal transcription pattern results from complex regulation of P_{ON}. **(b)** Transcriptional parameters for *gt* in male embryos during NC13 and NC14, plotted as a function of P_{ON} (orange), overlaid with data from all other gap genes (gray) for comparison. **(c)** Initiation rate K as a function of P_{ON}. Data collapse across all gap genes, time points, and positions reveals a shared K–P_{ON} relationship. Colored points correspond to individual genes (color code as in panel b and Fig. 4a–e); gray points represent pooled data from all other genes. The corresponding curve for *hb* is shown in Fig. 2h. **(d)** Near–steady-state relationship between P_{ON} and $T_{ON}/(T_{ON}+T_{OFF})$, shown for all gap genes in NC13 ($t \geq 6.5$ min) and NC14 ($t \geq 7.5$ min). While most data points follow the expected relationship (dashed line), a slight but consistent bias appears at the extremes of the P_{ON} range (solid line): $T_{ON}/(T_{ON}+T_{OFF})$ slightly exceeds zero at $P_{ON}=0$ and slightly undershoots one at $P_{ON}=1$. This bias arises from the finite duration of our recordings (18.4 min in NC13 and 50 min in NC14), which imposes an upper bound on the detectable lengths of ON and OFF intervals, thereby affecting the estimates near the boundaries of P_{ON}.

https://doi.org/10.1038/s41594-025-01615-4

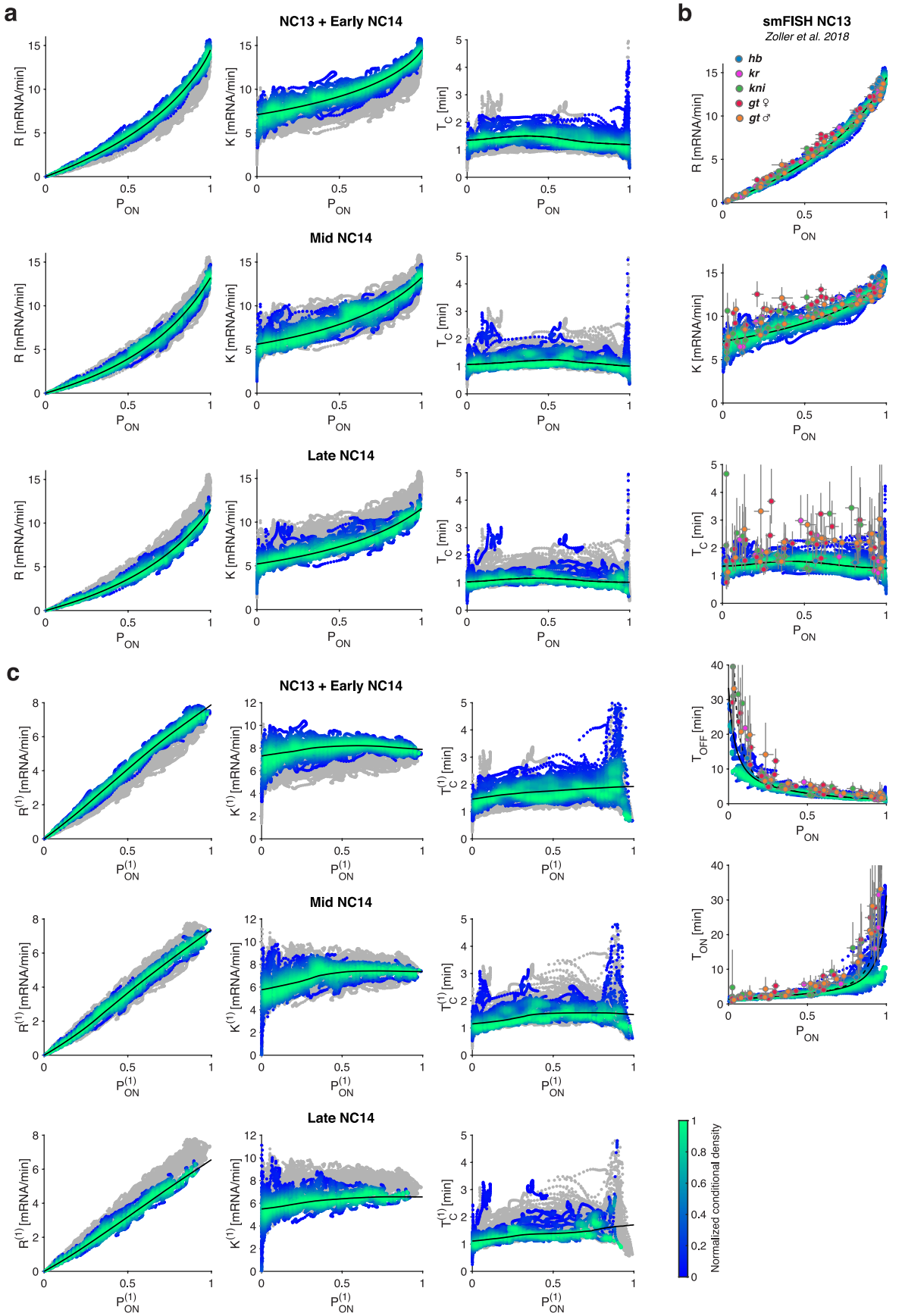

Extended Data Fig. 8 | See next page for caption.

https://doi.org/10.1038/s41594-025-01615-4

Extended Data Fig. 8 | Common bursting relationships across developmental time and for single gene copy. (a) Global scatter of effective transcriptional parameters as a function of P_{ON}, estimated for all gap genes across three developmental time windows: NC13 ($6.5 \le t$ min) plus early NC14 ($7.5 \le t <$ 20.5 min), mid NC14 ($20.5 \le t < 34.5$ min), and late NC14 ($34.5 \le t < 48$ min). Due to the high degree of nuclear synchronization in the blastoderm embryo (with respect to the cell cycle), it is possible to assess global temporal changes by comparing these windows. The bursting relationships are further refined when accounting for temporal changes (color scatter), compared to time-pooled data (gray scatter, Fig. 5a). Modest developmental decreases in K and T_C (~40%) help explain part of the spread observed in Fig. 5a. The origin of these changes remains unclear but may reflect overall temporal regulation of the gap gene network or maternal-to-zygotic transitions previously associated with mid-NC14. **(b)** Bursting relationships inferred from NC13 and early NC14 data are consistent with parameters previously derived from fixed smFISH measurements [23]. We converted mid-to-late NC13 single gene copy (SGC) parameters from smFISH into effective two-chromatid parameters (colored points), with 68% confidence intervals. The resulting effective correlation time from smFISH, $T_C = 2.06 \pm 0.66$ min, is slightly shorter than reported in the original study ($T_C = 3.0 \pm 1.2$ min). This discrepancy arises from two corrections: (1) our updated elongation rate of 1.8 kb/min (versus 1.5 kb/min previously) reduces T_C by 17%, and (2) the effective correlation time becomes up to twofold shorter than the SGC correlation time $T_C^{(1)}$ at high P_{ON}, due to the relationship $T_C^{(1)} = 2\,T_C/(1 + (1 - P_{ON})^{1/2})$, (see Methods), accounting for an additional ~17% decrease on average. Overall, the smFISH effective parameters closely verify our relationships derived from live measurements ($T_C = 2.06 \pm 0.66$ min fixed versus $T_C = 1.25 \pm 0.37$ min live), albeit with small deviations likely stemming from a technical origin (differences in experimental protocol and microscopy, as well as limitations imposed by fixed measurements on parameter estimation). These small deviations, along with simulations (Supplementary Figs. 1 and 2), suggest that the observed data spread is largely attributable to estimation uncertainty rather than biological variability. **(c)** Same as in (**a**), but showing SGC parameters inferred from effective measurements under the assumption of independent sister chromatids (see Supplementary Fig. 4 for weakly correlated case with $\rho = 0.16$). The differences between the independent and weakly correlated assumptions are minor. Notably, in both cases, the relationship between SGC transcription rate $R^{(1)}$ and SGC ON-probability $P_{ON}^{(1)}$ is nearly linear, supporting the conclusion that $K^{(1)}$, the SGC initiation rate, is largely independent of $P_{ON}^{(1)}$. Thus, the apparent dependence of effective K on P_{ON} arises as an emergent property of two-gene-copy measurements, not from intrinsic single-copy regulation.

https://doi.org/10.1038/s41594-025-01615-4

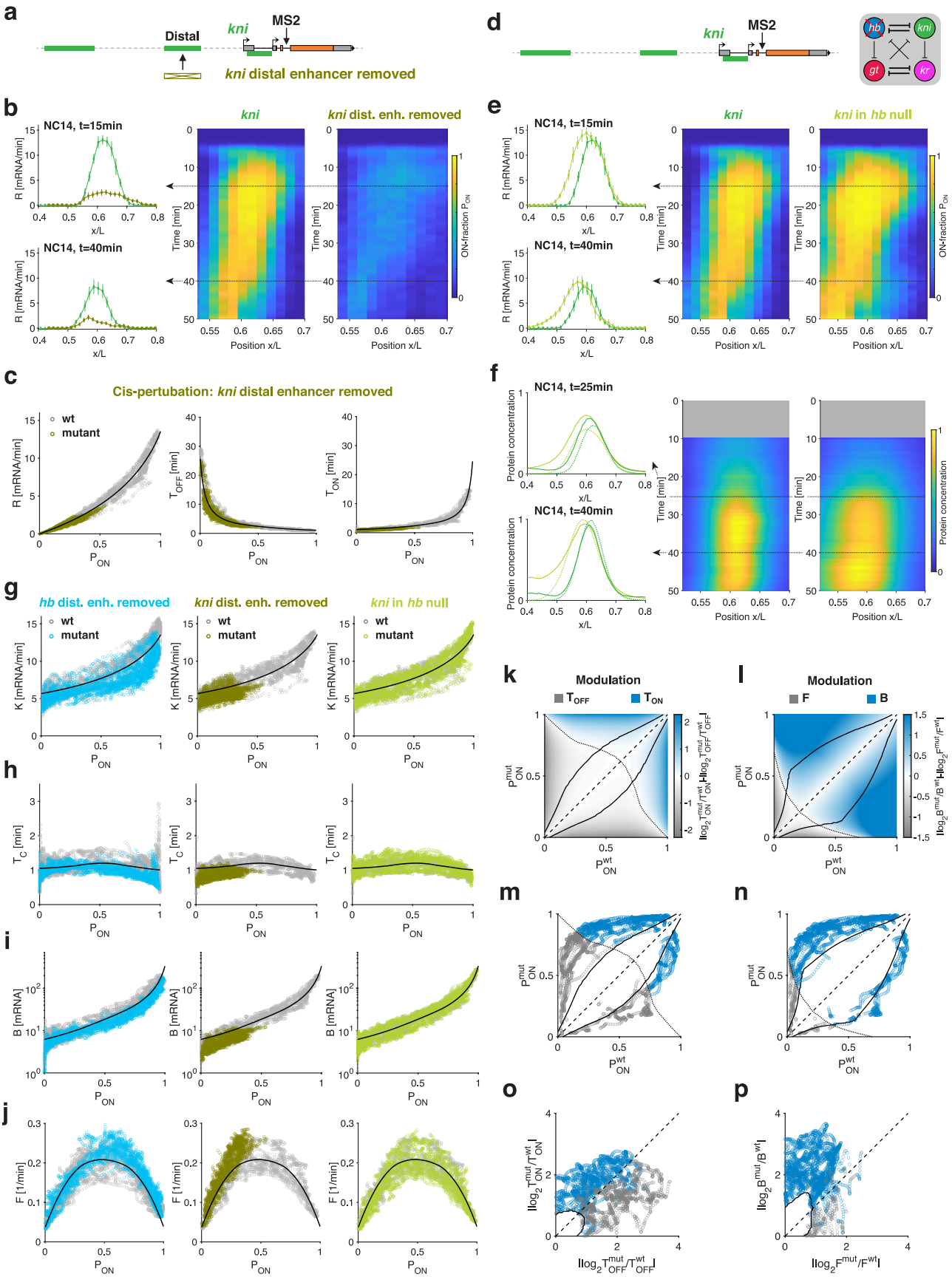

Extended Data Fig. 9 | See next page for caption.

https://doi.org/10.1038/s41594-025-01615-4

Extended Data Fig. 9 | Bursting relationships verified by *cis*- and *trans*-perturbations. (a) Cis-regulatory mutant for *kni*: deletion of the distal *kni* enhancer. MS2 stem-loops are inserted at the same genomic position in both the mutant and wild-type fly lines. **(b)** Quantification of transcriptional phenotypes for *kni* wild-type and cis-mutant. The transcription rate R as a function of position x/L (left) and the kymograph of P_{ON} (right) both show a pronounced reduction in expression in the mutant. The dotted arrow indicates the time point in the kymograph corresponding to the rate profiles on the left. Error bars denote ±1 standard deviation across embryo means. **(c)** Transcriptional parameters for the *kni* cis-mutant (olive) collapse onto the corresponding wild-type relationships (gray), as observed for the *hb* cis-mutant (Fig. 6c). Solid black lines show the endogenous bursting relationships from Fig. 5a, b. **(d)** Trans-regulatory mutant: *kni*-MS2 measured in a *hb* null background. In the absence of *hb*, the regulatory network is altered, which in turn affects the concentrations of input transcription factors sensed by *kni*. **(e)** Quantification of *kni* transcription in wild-type and trans-mutant. Both the transcription rate R and P_{ON} kymograph exhibit a clear anterior shift in the mutant. The dotted arrow marks the time point at which rate profiles are extracted. Error bars indicate ±1 standard deviation across embryo means. **(f)** Comparison of *kni* expression at the protein level for wild-type and trans-mutant embryos, using staged antibody staining from Haroush et al., 2023[44]. While these measurements (solid lines, left) are not fully quantitative, they display a similar anterior shift in expression. Predicted protein profiles based on measured transcription rates (dashed lines, using the model from Extended Data Fig. 4) reproduce the same shift qualitatively. **(g–j)** Bursting parameters, initiation rate K (**g**), correlation time T_C (**h**), burst size B (**i**), and burst frequency F (**j**), for *hb* cis-mutant (cyan), *kni* cis-mutant (olive), and *kni* trans-mutant (light green) collapse onto the wild-type trends (gray). Solid black lines represent wild-type bursting relationships (Fig. 5a–c). **(k–p)** Predicting mutant modulation type based on wild-type-derived bursting relationships (Fig. 5a–c). Mutant bursting behavior, whether modulated through T_{OFF} vs. T_{ON}, or F vs. B, is predicted using look-up tables from wild-type data. **(k)** Predicted modulation type using T_{OFF} and T_{ON}. For each mutant–wild-type pair of P_{ON} values, the expected fold changes $T_{OFF}^{mut}/T_{OFF}^{wt}$ and T_{ON}^{mut}/T_{ON}^{wt} are computed based on wild-type relationships. The dotted line separates regimes where changes in R are driven primarily by T_{OFF} (gray region: $|\log T_{OFF}^{mut}/T_{OFF}^{wt}| > |\log T_{ON}^{mut}/T_{ON}^{wt}|$) or T_{ON} (blue region: opposite inequality). Solid black lines bound regions where neither change is significant, based on 95% confidence intervals. This framework forms a look-up table for predicting modulation type from P_{ON} pairs. **(l)** Same as (**k**), but using burst frequency F and burst size B instead of T_{OFF} and T_{ON}. **(m)** Scatter plot of all P_{ON} pairs from *hb* wild-type and cis-mutant at matched spatiotemporal positions. Color indicates the predicted modulation type (gray: T_{OFF}-dominated; blue: T_{ON}-dominated), based on the look-up table in (**k**). **(n)** Same as (**m**), but using F and B modulation types from panel (**l**). **(o)** Empirical verification of predictions in (**k**). For each P_{ON} pair, we compute fold changes in $T_{OFF}^{mut}/T_{OFF}^{wt}$ and T_{ON}^{mut}/T_{ON}^{wt} from the data (Fig. 6c, d). Nrly all blue points (predicted T_{ON}-modulation) lie above the diagonal (slope 1, dashed), while gray points (predicted T_{OFF}-modulation) lie below, yielding >85% prediction accuracy (Fig. 6e). **(p)** Same as (**o**), using F and B instead of T_{OFF} and T_{ON}. Predictions are highly accurate: >95% of data points fall in the expected quadrants (Fig. 6g), validating the predictive framework.

https://doi.org/10.1038/s41594-025-01615-4

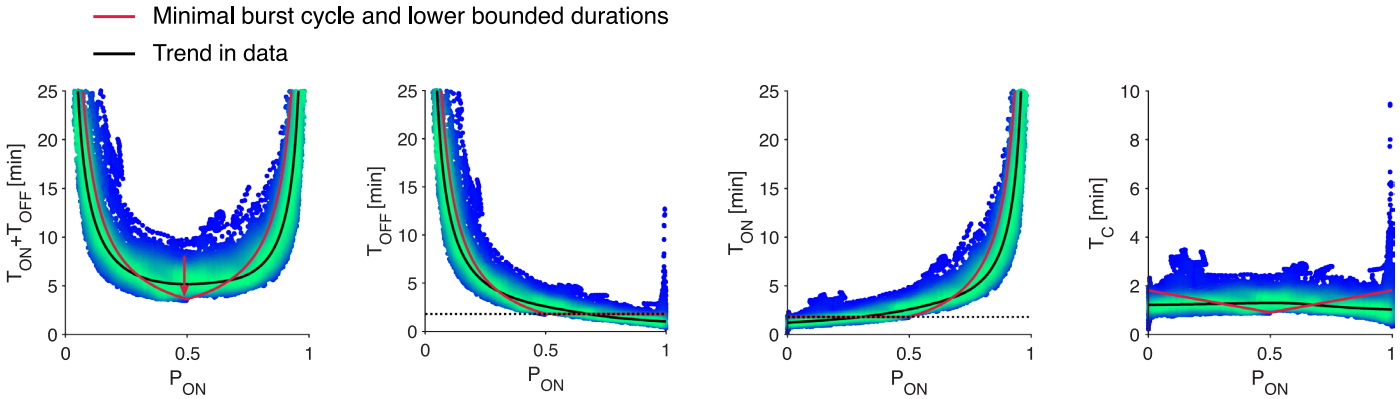

Extended Data Fig. 10 | A bursting regime with a minimal ON-OFF cycle recapitulated the data. An ON-OFF transcriptional regime, with a lower limit on these period durations and a minimal mean burst cycle duration $T_{ON} + T_{OFF} = 1/F$ shown in red, closely recapitulates the observed bursting relationships in black. The horizontal dotted line corresponds to a lower bound of 1.8 min providing the best-fit to the data. An allele at mid-activity level ($P_{ON} = 0.5$) minimizes $T_{ON} + T_{OFF}$. Various ON-OFF combinations can yield $P_{ON} > 0.5$, but increasing OFF periods prolong encoding P_{ON} compared to solely increasing ON durations.

nature portfolio

Corresponding author(s): Thomas Gregor

Last updated by author(s): May 15, 2025

Reporting Summary

Nature Portfolio wishes to improve the reproducibility of the work that we publish. This form provides structure for consistency and transparency in reporting. For further information on Nature Portfolio policies, see our Editorial Policies and the Editorial Policy Checklist.

Statistics

For all statistical analyses, confirm that the following items are present in the figure legend, table legend, main text, or Methods section.

n/a	Confirmed	
☐	☒	The exact sample size (*n*) for each experimental group/condition, given as a discrete number and unit of measurement
☐	☒	A statement on whether measurements were taken from distinct samples or whether the same sample was measured repeatedly
☒	☐	The statistical test(s) used AND whether they are one- or two-sided *Only common tests should be described solely by name; describe more complex techniques in the Methods section.*
☐	☒	A description of all covariates tested
☐	☒	A description of any assumptions or corrections, such as tests of normality and adjustment for multiple comparisons
☐	☒	A full description of the statistical parameters including central tendency (e.g. means) or other basic estimates (e.g. regression coefficient) AND variation (e.g. standard deviation) or associated estimates of uncertainty (e.g. confidence intervals)
☒	☐	For null hypothesis testing, the test statistic (e.g. *F*, *t*, *r*) with confidence intervals, effect sizes, degrees of freedom and *P* value noted *Give P values as exact values whenever suitable.*
☐	☒	For Bayesian analysis, information on the choice of priors and Markov chain Monte Carlo settings
☐	☒	For hierarchical and complex designs, identification of the appropriate level for tests and full reporting of outcomes
☐	☒	Estimates of effect sizes (e.g. Cohen's *d*, Pearson's *r*), indicating how they were calculated

Our web collection on statistics for biologists contains articles on many of the points above.

Software and code

Policy information about availability of computer code

Data collection	Custom 2-photon acquisition software, Zeiss LSM 880 -Zen software 2.3SP1
Data analysis	Matlab 2023b codes were used to analyze all our data; they are fully available on GitLab (https://gitlab.pasteur.fr/tglab/liveburstrulepaper).

For manuscripts utilizing custom algorithms or software that are central to the research but not yet described in published literature, software must be made available to editors and reviewers. We strongly encourage code deposition in a community repository (e.g. GitHub). See the Nature Portfolio guidelines for submitting code & software for further information.

Data

Policy information about availability of data

All manuscripts must include a data availability statement. This statement should provide the following information, where applicable:

- Accession codes, unique identifiers, or web links for publicly available datasets
- A description of any restrictions on data availability
- For clinical datasets or third party data, please ensure that the statement adheres to our policy

Original movies are available upon request. Full processed datasets are provided as Source data and available on Zenodo (https://doi.org/10.5281/zenodo.15396339).

Research involving human participants, their data, or biological material

Policy information about studies with human participants or human data. See also policy information about sex, gender (identity/presentation), and sexual orientation and race, ethnicity and racism.

Reporting on sex and gender	N.A.
Reporting on race, ethnicity, or other socially relevant groupings	N.A.
Population characteristics	N.A.
Recruitment	N.A.
Ethics oversight	N.A.

Note that full information on the approval of the study protocol must also be provided in the manuscript.

Field-specific reporting

Please select the one below that is the best fit for your research. If you are not sure, read the appropriate sections before making your selection.

☒ Life sciences ☐ Behavioural & social sciences ☐ Ecological, evolutionary & environmental sciences

For a reference copy of the document with all sections, see nature.com/documents/nr-reporting-summary-flat.pdf

Life sciences study design

All studies must disclose on these points even when the disclosure is negative.

Sample size	No statistical method was used to predetermine sample size. Between 10 and 20 embryos measured per condition leading to statistical estimates that are largely within the 95% confidence interval.
Data exclusions	No outliers removed unless clear experimental flaws were identified.
Replication	Experiments were performed over several months across a two-year period, consistently yielding healthy embryos suitable for imaging.
Randomization	Embryos were assigned to groups based on known genotypes from controlled breeding, so randomization of group allocation was not applicable.
Blinding	Blinding was not relevant because imaging and quantification procedures were standardized, identical across conditions, and not influenced by group assignment.

Reporting for specific materials, systems and methods

We require information from authors about some types of materials, experimental systems and methods used in many studies. Here, indicate whether each material, system or method listed is relevant to your study. If you are not sure if a list item applies to your research, read the appropriate section before selecting a response.

Materials & experimental systems

n/a	Involved in the study
☒	☐ Antibodies
☒	☐ Eukaryotic cell lines
☒	☐ Palaeontology and archaeology
☐	☒ Animals and other organisms
☒	☐ Clinical data
☒	☐ Dual use research of concern
☒	☐ Plants

Methods

n/a	Involved in the study
☒	☐ ChIP-seq
☒	☐ Flow cytometry
☒	☐ MRI-based neuroimaging

Animals and other research organisms

Policy information about studies involving animals; ARRIVE guidelines recommended for reporting animal research, and Sex and Gender in Research

Laboratory animals	Species: Drosophila melanogaster; Oregon-R, BDSC#78781 and BDSC#78782 strains, Sex: mixed; Age: 1-3h embryos
Wild animals	No wild animals were used in the study
Reporting on sex	Sex is reported for genes on X chromosome
Field-collected samples	No field collected samples were used in the study
Ethics oversight	No ethical approval was necessary

Note that full information on the approval of the study protocol must also be provided in the manuscript.

Plants

Seed stocks	N.A.
Novel plant genotypes	N.A.
Authentication	N.A.